A Numerical Experiment on the Interactions of Radiation, Clouds and Dynamic Processes in a General Circulation Model

KUO-NAN LIOU AND QINGLIN ZHENG[1]

Department of Meteorology, University of Utah, Salt Lake City, UT 84112

(Manuscript received 30 June 1983, in final form 13 February 1984)

ABSTRACT

Physical interactions of radiation, cloud formation and dynamic processes are investigated utilizing a general circulation model designed for short and medium range prediction. The present model is a seven-level spectral model in the σ-coordinate system for the Northern Hemisphere with the generation of clouds in four σ layers through the predicted relative humidity field. Computations of the cloud liquid water content involving various cloud combinations for radiation transfer analyses are based on assumed particle size distributions assigned to cumulus, stratus, altostratus, cumulonimbus and cirrus. Parameterization of the thermal IR and solar flux transfer in a clear atmosphere utilizes the broadband emissivity (IR) and absorptivity (solar) concept for water vapor, ozone and carbon dioxide emission and absorption. Broadband solar flux reflection and transmission for various cloud types as functions of the liquid water content, solar zenith angle and average cloud temperature under a number of model conditions are parameterized in line with the gaseous broadband absorptivity. Moreover, high clouds are considered to be nonblack whose parameterized emissivity is expressed in terms of the vertical ice content. We have physically described and mathematically quantized the effects of radiative processes on the vertical velocity, temperature and cloud field (via the water vapor mixing ratio) by virtue of the fundamental equations governing these variables in the model. We demonstrate, through the predicted vertical velocity for the fifth day, that radiative flux exchanges in the tropics lead to a significant intensification of the Hadley circulation and that such processes also strengthen to some degree the meridional circulation. In addition, we show that the part of the vertical velocity produced by radiative processes represents a significant component in the tropical region, whereas it is only about 10–15% of the total in middle and high latitudes. Moreover, we also discover a consistent and characteristic pattern involving warm and cold advections of temperature associated with frontal activities and the part of the vertical velocity produced by radiative flux exchanges. In areas associated with high and low temperature advections radiative processes appear to enhance and suppress the upward motion, respectively. With verification from the satellite IR cloud picture we show that the present model performs quite realistically on the prediction of cloud cover. When radiative processes were not incorporated in the model, however, the cloud cover in the tropics is underestimated by as much as 50% due to the lack of the low cloud formation. Furthermore, we show that the present model with interactive radiative processes has improved the temperature prediction by about 1–2°C in middle latitudes and <1°C in the tropics. Statistical analyses show that this improvement is significant in low levels. Finally, we illustrate that the present model predicts accurately the mean 500 mb temperatures for nine consecutive days utilizing a data set covering the period from 7 to 15 June 1980.

1. Introduction

Almost all the energy that drives the earth's atmosphere and ocean currents originates from the sun. The land and ocean surfaces absorb about 46% of the incoming solar fluxes while the atmosphere absorbs about another 23% of these fluxes. When the temperature of the earth–atmosphere system consisting of molecules and particulates is structured, the outgoing thermal infrared fluxes are emitted, and over a period of a sufficiently long time, the absorbed solar fluxes will be balanced by the emitted thermal infrared fluxes. Radiative processes are the only means by which the earth and atmosphere exchange energy with space. Within the atmosphere, water vapor undergoes thermodynamic phase transitions which are governed by the laws of thermodynamics and dynamics for various scales of motion. These transitions lead to the formation and dissipation of water and ice clouds and precipitation processes. The ocean covers about 70% of the earth's surface. It absorbs a large portion of solar fluxes impinging on it and, meanwhile, provides the necessary and sufficient water substance to the atmosphere for the formation of cloud systems in the troposphere. Thus, the evolution and distribution of water vapor and clouds when coupled with radiative processes play the most significant role in the energetic and general circulation of the atmosphere. The importance of the coupling of radiative processes and hydrological cycles in the context of numerical modeling for weather prediction and climate solution(s) has been well recognized and acknowledged physically and dynamically.

[1] On leave from the Academy of Meteorological Science, National Meteorological Bureau, Beijing, China.

Several pioneering investigations have been aimed at the understanding of the impact of radiation and cloud processes on the sensitivity of the atmospheric structure using general circulation models. Wetherald and Manabe (1980) studied the sensitivity of the area-mean temperature of the model to the variation of cloud cover based on the results from general circulation experiments. They noted that cloud cover, on the one hand, reflects incoming solar fluxes and exerts a cooling effect on climate, and on the other, it traps outgoing thermal infrared fluxes and contributes to climatic warming. Kuo and Qian (1981) investigated the dynamic and thermodynamic influences of the Tibetian Plateau on the monsoon circulation and the climate of Asia utilizing a simplified general circulation model. They illustrated the significance of the thermal effects, including radiative and cloud processes, on the distribution of the temperature and geopotential height field in the Tibetian region. More recently, Ramanathan *et al.* (1983) demonstrated the possibility of improving the mean zonal simulation by virtue of refinements and improvements in radiative processes within the context of a general circulation model. Specifically, they showed that the radiative properties of cirrus clouds may have a direct impact on the general circulation of the atmosphere.

Although the relative importance of radiative–cloud processes on the climate problem has been physically realized, the relevance of these processes to medium range weather prediction and the extent and degree to which prediction improvements by the consistent integration of these processes in the model can be made are questions still open for scientific investigation and debate. In conjunction with this, several unpublished papers that appeared in the report issued by the European Centre for Medium Range Weather Forecasts (see, e.g., Geleyn, 1981) offer some pioneering analyses of radiation and radiation–cloud processes in numerical modeling for medium range weather prediction.

In this paper, we attempt to understand the intricate interactions of radiation, clouds and dynamic processes in a general circulation model that is realistic and suitable for the performance of short and medium range weather prediction. The present model is a modification and improvement of the four-level spectral model originally developed by Zheng (1981) with the consistent incorporation of a newly developed radiation and cloud parameterization program based on numerous previous studies (Liou and Wittman, 1979; Liou and Ou, 1981, 1983; Ou and Liou, 1983). In Section 2, we describe the seven-level spectral general circulation in the σ-coordinate including the method of solution to the fundamental set of dynamic and thermodynamic equations and the empirical and physical scheme for the formation of clouds in the model. Next, we present the newly developed thermal infrared and solar radiation programs for clear and cloudy atmospheres in line with the model structure based on the concept of the broadband flux transfer. Simulation results are subsequently illustrated and discussed physically. We first present heating and cooling profiles and cloud cover values computed from the model. Possible direct and indirect interactions between radiation, vertical velocity, temperature, clouds, humidity and large-scale motions are then described. Quantitative effects of radiative processes on the vertical velocity and general circulation of the atmosphere and on the cloud and temperature predictions are demonstrated and documented. Finally, in light of the model results, a number of conclusions and prospects for further research are given in Section 5.

2. The spectral general circulation model

Spectral models have recently emerged as an attractive means of simulating the general circulation of the atmosphere (Bourke *et al.*, 1977; Manabe *et al.*, 1979; Zheng, 1979; Pitcher *et al.*, 1983). The advantages of the spectral method in relation to the finite-difference method have been shown to be the elimination of aliasing, the accuracy of horizontal advection computations, and the ease of global modeling in which a semi-implicit time integration scheme can be incorporated. However, the spectral method encounters difficulties in the computation of nonlinear terms. These difficulties appear to be largely resolved through the advent of transform methods proposed by Orszag (1970). One of the present authors (Zheng) in 1971 has independently proposed a technique for calculating nonlinear terms in a one-level spectral model in which a spectral method was employed accurately along the latitude and a pseudo-spectral method was adopted along the longitude. Subsequently, such a technique was successfully applied to a three-level filtered spectral model (Zheng, 1979) and a seven-level primitive equation spectral model (Zheng, 1980). The spectral general circulation model used for the present study of the interactions of radiation, clouds and dynamic processes is largely based on four-level and seven-level spectral models developed by Zheng (1980, 1981). However, significant modifications and improvements on the model and to the σ-coordinate system have been carried out.

a. The model

The present general circulation model designed for short and medium range weather prediction consists of seven levels in the σ-coordinate as shown in Fig. 1. The basic system of dynamic and thermodynamic equations expressed in the σ-coordinate for the model may be described as follows:

$$\frac{\partial u}{\partial t}+\frac{u}{a\sin\theta}\frac{\partial u}{\partial \lambda}+\frac{v}{a}\frac{\partial u}{\partial \theta}+\dot{\sigma}\frac{\partial u}{\partial \sigma}+fv+\frac{uv}{a}\cot\theta$$
$$=-\frac{1}{a\sin\theta}\frac{\partial \phi}{\partial \lambda}-\frac{RT}{a\sin\theta}\frac{\partial \ln P_*}{\partial \lambda}+F^u+\frac{g}{P_*}\frac{\partial \tau^u}{\partial \sigma}, \tag{2.1}$$

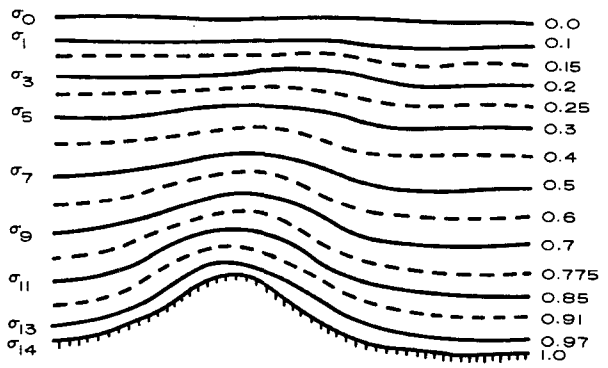

FIG. 1. The vertical structure of the spectral general circulation model in the σ-coordinate.

$$\frac{\partial v}{\partial t}+\frac{u}{a\sin\theta}\frac{\partial v}{\partial\lambda}+\frac{v}{a}\frac{\partial v}{\partial\theta}+\dot{\sigma}\frac{\partial v}{\partial\sigma}-fu-\frac{u^2}{a}\cot\theta$$
$$=-\frac{1}{a}\frac{\partial\phi}{\partial\theta}-\frac{RT}{a}\frac{\partial\ln P_*}{\partial\theta}+F^v+\frac{g}{P_*}\frac{\partial\tau^v}{\partial\sigma}, \quad (2.2)$$

$$\frac{\partial T}{\partial t}+\frac{u}{a\sin\theta}\frac{\partial T}{\partial\lambda}+\frac{v}{a}\frac{\partial T}{\partial\theta}-\left(\frac{RT}{C_p\sigma}-\frac{\partial T}{\partial\sigma}\right)\dot{\sigma}$$
$$-\frac{RT}{C_p}\frac{d\ln P_*}{dt}=-\frac{F\delta L\hat{\omega}}{C_pa^2}+Q^R+F^T+\frac{g}{P_*}\frac{\partial\tau^T}{\partial\sigma}, \quad (2.3)$$

$$\frac{\partial q}{\partial t}+\frac{u}{a\sin\theta}\frac{\partial q}{\partial\lambda}+\frac{v}{a}\frac{\partial q}{\partial\theta}+\dot{\sigma}\frac{\partial q}{\partial\sigma}=\frac{F\delta\hat{\omega}}{a^2}+F^q+\frac{g}{P_*}\frac{\partial\tau^q}{\partial\sigma}, \quad (2.4)$$

$$\frac{1}{a\sin\theta}\left[\frac{\partial u}{\partial\lambda}+\frac{\partial(v\sin\theta)}{\partial\theta}\right]+\frac{\partial\dot{\sigma}}{\partial\sigma}+\frac{d\ln P_*}{dt}=0, \quad (2.5)$$

$$T=-\frac{\sigma}{R}\frac{\partial\phi}{\partial\sigma}, \quad (2.6)$$

$$\frac{\partial\ln P_*}{\partial t}=-\int_0^1\left\{\frac{1}{a\sin\theta}\left[\frac{\partial u}{\partial\lambda}+\frac{\partial(v\sin\theta)}{\partial\theta}\right]\right.$$
$$\left.+\frac{u}{a\sin\theta}\frac{\partial\ln P_*}{\partial\lambda}+\frac{v}{a}\frac{\partial\ln P_*}{\partial\theta}\right\}d\sigma, \quad (2.7)$$

$$\hat{\omega}=a^2(\dot{\sigma}/\sigma+\dot{P}_*/P_*), \quad \omega=\sigma P_*\hat{\omega}/a^2. \quad (2.8)$$

In these basic equations, $\theta = 90° -$ latitude, λ is the longitude, a the radius of the earth, $\sigma = P/P_*$ with P_* the pressure at the surface, R the universal constant for air, C_p the specific heat at constant pressure, L the latent heat per unit mass, and other basic notations are conventional. Eq. (2.7) is derived by using the boundary conditions that $\dot{\sigma} = 0$ at $\sigma = 0$ and 1.

The delta function has been introduced in Eqs. (2.3) and (2.4) such that

$$\delta=\begin{cases}h_c & \text{for } \omega<0 \text{ and } q\geq q_c\\ 0 & \text{for } \omega\geq 0 \text{ or } q<q_c,\end{cases} \quad (2.9)$$

where the critical relative humidity $h_c = q_c/q_s$, and q_s and q_c are the saturation and critical mixing ratio with the former a function of temperature only. The critical relative humidity is generated in the model through Eq. (2.29) discussed in Subsection 2c. Moreover, in the equations for the temperature and humidity F is given by

$$F=q_sT(LR-C_pR_vT)/(C_pR_vT^2+q_sL^2), \quad (2.10)$$

where R_v is the universal constant for water vapor. This equation may be derived from the first law of thermodynamics for saturation adiabatic processes, the Clausius–Clapeyron equation and the definition of the saturation mixing ratio. The first term on the right-hand side of Eq. (2.3) represents the heating from the large-scale condensation process. And the radiative heating term denoted in Eq. (2.3) in the σ-coordinate may be written in the form

$$Q_R=\frac{g}{P_*C_p}\frac{\partial}{\partial\sigma}(F_S-F_{IR}), \quad (2.11)$$

where F_S and F_{IR} represent the net solar and thermal infrared fluxes to be discussed more comprehensively in Section 3.

The vertical diffusion terms denoted in Eqs. (2.1)–(2.4) are taken to be

$$\tau^{(u,v)}=\begin{cases}-\rho C_D|\mathbf{v}|(u,v), & \sigma=1\\ \tilde{K}\dfrac{\partial(u,v)}{\partial\sigma}, & \sigma<1,\end{cases} \quad (2.12)$$

$$\tau^T=\begin{cases}-\rho C_D|\mathbf{v}|[T(z_1)-T_*], & \sigma=1\\ 0, & \sigma<1,\end{cases} \quad (2.13)$$

$$\tau^q=\begin{cases}-\rho C_D|\mathbf{v}|[q(z_1)-q_s(T_*)], & \sigma=1\\ \tilde{K}\dfrac{\partial q}{\partial\sigma}, & \sigma<1,\end{cases} \quad (2.14)$$

where the eddy viscosity is defined by the mixing length theory in the form

$$\tilde{K}=\tilde{K}_1\bar{l}^2\frac{\partial|\mathbf{v}|}{\partial\sigma}. \quad (2.15)$$

In Eqs. (2.12)–(2.15), $\tilde{K}_1 = \rho^3(g/P_*)^2$, $\bar{l}$ the mixing length which is a function of σ, $z_1 = z + 75$m, z the terrain height and C_D the drag coefficient which is a function of the surface characteristics and terrain height. The horizontal eddy nonlinear viscosity terms for u, v, temperature and humidity components are denoted by F^u, F^v, F^T and F^q, respectively. Equations for the computations of these terms follow those presented by Smagorinsky (1963) and will not be duplicated here.

In this model, the surface temperature T_* is calculated from the following heat budget equation at the surface:

$$F_s^* = \tilde{\sigma}T_*^4 - F_{IR}^* + C_p\tau_*^T + L\tau_*^q + C_p\hat{\tau}_*^T + B_2(T_* - T_\Delta), \quad (2.16)$$

where F_s^* is the absorbed solar flux at the surface, F_{IR}^* the downward thermal infrared flux from the atmosphere to the surface, $\tilde{\sigma}T_*^4$ the upward blackbody thermal infrared flux from the surface, $\tilde{\sigma}$ the Stefan–Boltzmann constant, $L\tau_*^q$ and $C_p\tau_*^T$ the latent and sensible heat fluxes from the surface to the atmosphere given in Eqs. (2.13) and (2.14), $C_p\hat{\tau}_*^T = B_1C_p\tau_*^T$, the heat flux due to conduction, the last term represents the heat flux from the melting ice, B_1 and B_2 denote the empirical constants and T_Δ is the melting temperature. The ocean temperatures are fixed in the model, however.

Convective adjustments are carried out in the model when the atmospheric lapse rate γ is greater than the dry adiabatic lapse rate γ_d coupled with the downward vertical velocity, or when γ is greater than the moist adiabatic lapse rate γ_m and the vertical velocity is upward. Before and after the dry or moist adiabatic adjustment, it is assumed that

$$\int_{\sigma_T}^{\sigma_B} Td\sigma = \text{constant},$$

where σ_T and σ_B denote the top and bottom of the unstable layer.

b. Solution method and computational aspect

On the basis of Eqs. (2.1) and (2.2), and after a series of mathematical operations, the equations of motions may be expressed in terms of vorticity ζ and divergence D in the $(\theta, \lambda, \sigma, t)$ coordinate system as follows:

$$\frac{\partial}{\partial t}(a^2\nabla^2\psi) + f(a^2\nabla^2\chi) = E^A + L^A, \quad (2.17)$$

$$\frac{\partial}{\partial t}(a^2\nabla^2\chi) - f(a^2\nabla^2\psi) + a^2\nabla^2\phi = E^B + L^B, \quad (2.18)$$

where $\zeta = \nabla^2\psi$, $D = \nabla^2\chi$, ψ and χ denote the streamfunction and velocity potential, respectively, E^A and E^B represent the nonlinear terms in the vorticity and divergence equations and L^A and L^B are the corresponding linear terms defined by Zheng (1981).

Moreover, from the computational aspect, we rewrite Eqs. (2.3) and (2.5) in the forms:

$$\frac{\partial T}{\partial t} - \tilde{\lambda}(a^2\dot{\sigma}) = E^T, \quad (2.19)$$

$$a^2\nabla^2\chi + \frac{\partial}{\partial\sigma}(a^2\dot{\sigma}) = E^f - \hat{E}^f, \quad (2.20)$$

where

$$\tilde{\lambda} = \left(\frac{R}{C_p}\frac{\tilde{T}}{\sigma} - \frac{\partial\tilde{T}}{\partial\sigma}\right)\Big/a^2,$$

with $\tilde{T}$ the averaged temperature over the longitude and co-latitude, E^T represents the sum of the terms denoted in Eq. (2.3) other than those written in the left-hand side of Eq. (2.19) and

$$E^f = -\frac{au}{\sin\theta}\frac{\partial}{\partial\lambda}\ln P_* - av\frac{\partial}{\partial\theta}\ln P_*, \quad (2.21a)$$

$$\hat{E}^f = \int_0^1 (-a^2\nabla^2\chi + E^f)d\sigma. \quad (2.21b)$$

An inspection of Eqs. (2.17) and (2.18) reveals that the streamfunction ψ may be eliminated so that the resulting equation will consist of terms involving $\nabla^2\chi$ and $\nabla^2\phi$ only. Furthermore, by virtue of Eqs. (2.6) and (2.19), an equation relating $\nabla^2\phi$ and $\dot{\sigma}$ may be derived. By means of these two resulting equations it follows that $\nabla^2\chi$ and $\dot{\sigma}$ are connected by

$$\frac{\partial}{\partial\sigma}\left[\frac{\partial^2}{\partial t^2}(a^2\nabla^2\chi) + f^2(a^2\nabla^2\chi)\right] - \frac{\tilde{\lambda}Ra^2}{\sigma}\nabla^2(a^2\dot{\sigma}) = \frac{Ra^2}{\sigma}\nabla^2E^T + \frac{\partial}{\partial\sigma}\left[f(E^A + L^A) + \frac{\partial}{\partial t}(E^B + L^B)\right]. \quad (2.22)$$

The objective of the aforementioned analysis is to derive an equation containing $\dot{\sigma}$ without $\nabla^2\chi$ and $\nabla^2\psi$ terms. For this purpose, we define various time integration terms such that $0 = 0(\theta, \lambda, \sigma, t)$, $0^{t\pm\Delta t} = 0(\theta, \lambda, \sigma, t \pm \Delta t)$ and $0^\Delta = 0(\theta, \lambda, \sigma, t + \Delta t) - 0(\theta, \lambda, \sigma, t - \Delta t)$, where the symbol 0 may represent $\dot{\sigma}$, ψ, χ, T, q, E^A, E^B, E^T, L^A, L^B, etc. At this point, we utilize the semi-implicit time integration scheme and apply it to Eqs. (2.22) and (2.20). On eliminating terms involving $\nabla^2\chi^{t+\Delta t}$ leads to

$$-\lambda a^2\nabla^2(a^2\dot{\sigma}^{t+\Delta t}) - \frac{\partial^2}{\partial\sigma^2}(a^2\dot{\sigma}^{t+\Delta t}) = \frac{\Delta t^2R}{\alpha\sigma}a^2\nabla^2E^T + \frac{\Delta t}{\alpha}\frac{\partial}{\partial\sigma}\left[f\Delta t(E^A + L^{A,t+\Delta t}) + E^B - E^{B,t-\Delta t} + \frac{1}{2}L^{B,\Delta} + \frac{a^2}{\Delta t}\nabla^2(2\chi - \chi^{t-\Delta t}) - \frac{\alpha a^2}{\Delta t}E^f\right], \quad (2.23)$$

where $\lambda = \Delta t^2R\tilde{\lambda}/(\alpha\sigma)$ and $\alpha = 1 + f^2\Delta t^2$. The same scheme may also be applied to Eqs. (2.20) and (2.17) to obtain

$$a^2\nabla^2\chi^{t+\Delta t} = -\frac{\partial}{\partial\sigma}(a^2\dot{\sigma}^{t+\Delta t}) + a^2(E^f - \hat{E}^f), \quad (2.24)$$

$$a^2\nabla^2\psi^\Delta = 2\Delta t[E^A + L^{A,t+\Delta t} - f(a^2\nabla^2\chi^{t+\Delta t})]. \quad (2.25)$$

Likewise, Eqs. (2.19), (2.4), (2.7) and (2.6) involving temperature, humidity, surface pressure and geopotential height may also be expressed in a similar manner.

The model utilizes the finite difference scheme in the vertical direction as shown in Fig. 1. However, in solving the system of equations, Eq. (2.23), involving

the vertical velocity, is computed at level σ_j (j = 2, 4, · · ·) while all other equations are computed at level σ_j (j = 1, 3, · · ·). Since the right-hand sides of Eqs. (2.23)–(2.25) contain $\dot{\sigma}^{t+\Delta t}$, $\chi^{t+\Delta t}$ and $\psi^{t+\Delta t}$ which are to be solved computationally, it is necessary to employ the iteration method to find solutions for them. Based on numerical experimentations, less than six iterations are sufficient to converge the solution with a high degree of accuracy. Subsequently, all other prediction parameters may be computed at the time step $t + \Delta t$. All the basic parameters in the model may be expanded by means of spherical harmonics in the form

$$0_j = \sum_{m=0}^{M} \sum_{n=1}^{N} (A^0_{j,m,m+2n-k} \cos m\lambda + B^0_{j,m,m+2n-k} \sin m\lambda) \times \bar{P}^m_{m+2n-k}(\cos\theta), \quad (2.26)$$

where $k = 1$ when the notation 0 represents the stream function ψ and $k = 2$, otherwise. The ranges of co-latitude θ and longitude λ are $0 \leqslant \theta \leqslant \pi/2$, $0 \leqslant \lambda \leqslant 2\pi$. A^0 and B^0 are unknown coefficients to be solved and $\bar{P}^m_{m+2n-k}$ denotes normalized associated Legendre polynomials. As a result of the spherical harmonics expansion, all nonlinear terms in the model may be computed efficiently and accurately (Zheng, 1981). For the sake of brevity, however, no further discussion will be made on the spectral method for the solution of the model equations.

c. *Cloud generation scheme*

The model allows partial or total cloud cover in four σ layers with values of 0.85, 0.7, 0.5 and 0.3. The cloud cover is calculated utilizing the relative humidity through the equation $h = q/q_s(T)$, where q and T are computed in the model. When the predicted relative humidity h is greater than a prescribed value, it is assumed that the water and/or ice cloud may be formed with the cloud cover computed from an empirical equation. On the other hand, if h is smaller than or equal to the prescribed value, no cloud is permitted to form in the model. Thus,

$$C = \begin{cases} g(h), & h > h_c \\ 0, & h \leqslant h_c, \end{cases} \quad (2.27)$$

where the function used in this study follows the scheme proposed by Geleyn (1981) in the form

$$g(h) = \frac{[h - h_c(\sigma)]^2}{[1 - h_c(\sigma)]^2} \quad (2.28)$$

and the critical relative humidity as a function of σ is given by

$$h_c(\sigma) = \sum_{n=0}^{3} a_n \sigma^n + \Delta h_c(\hat{\omega}), \quad (2.29)$$

where the a_n are empirical coefficients ($a_0 = 1$, $a_1 = -0.218$, $a_2 = -0.3196$, and $a_3 = 3.464$) and Δh_c is a correction factor (<0.04) which is empirically incorporated in this equation by inspecting the magnitude and sign of the vertical velocity $\hat{\omega}$ generated in the model.

All possible cloud locations in the model are depicted in Fig. 2 where indices 1–4 denote single cloud layer formations. When clouds form it is assumed that they fill the entire layer, except in the case of the high cloud. For this case, we assume that cirrus clouds are formed in the lower half of the layer. This assumption takes into consideration that the uppermost cloud layer in the model has a larger vertical geometric thickness. Middle clouds 1 and 2 and the low cloud are considered to be altostratus and stratus, respectively, consisting of entirely spherical water droplets. For radiative transfer calculations, ice particles within cirrus are assumed to be monodispersed and cylindrical in shape with a size of 200 and 60 μm in length and width, respectively (Heymsfield, 1975). Middle clouds (altostratus) and the low cloud (stratus) are assumed to have droplet size distributions reported by Diem (1948) and Singleton and Smith (1960). The volume liquid water/ice content of the three cloud types are depicted

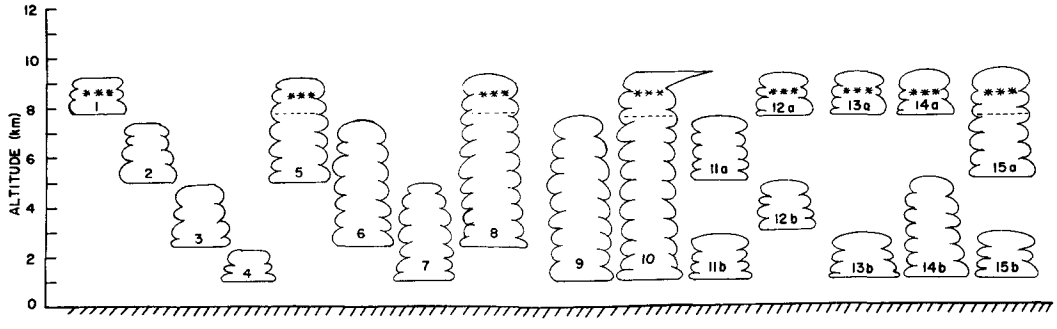

FIG. 2. Cloud formation in four σ layers in the model. All possible combinations of various cloud types are shown in the diagram. The asterisks denote ice crystal clouds (see text for further explanations).

in Table 1 based on observed values. In this table, the range of the droplet radius and the mean radius are also listed. It should be noted that the volume liquid water contents depicted in this table are the best data available in terms of mean values. (Of course, it would be ideal to have a data set derived from a consistent observational program.)

When two clouds are formed in the adjacent layers as depicted in cases 5, 6 and 7 in Fig. 2, we make the following cloud physics assumptions for the purpose of radiative transfer calculations. In case 5, we combine the broadband solar reflection and transmission values for the high cloud and middle cloud 1, which are considered to be separate cloud systems, based on a modified adding method described in the section dealing with the solar radiation program. It is important, from the point of view of radiative transfer, that ice clouds be treated independently from water clouds since the radiative properties of the former differ greatly from those of the latter. In case 6, cloud physics data used are the same as in the altostratus case. On the other hand, we consider clouds generated in the configuration of case 7 to be cumulus with a droplet size distribution and a mean liquid water content of 0.66 g m^{-3} presented by Durbin (1959).

Three adjacent and four layered clouds generated in the model are described by cases 8, 9 and 10 in Fig. 2. In case 8, the broadband solar radiative properties are derived from those of the high and middle cloud with their thicknesses provided by the model. Moreover, it is assumed that when clouds are formed in the three lowermost layers (cases 9 and 10), they are cumulonimbus. The droplet size distribution used in solar radiative transfer computations is based on observations of Weickmann and aufm Kampe (1953) with a liquid water content of 2.5 g m^{-3}. In the cloud generation model, whenever case 10 occurs and if vertical velocities in the four σ layers are upward, the cloud cover is assumed to be 100%. This case can be thought of as a case of deep convection discussed by House and Cheng (1981). In addition to the above-mentioned cloud cases, there are five possible multiple cloud systems with air in between as illustrated in Fig. 2, cases 11–15. Considerations of cloud droplet/ice crystal particle size distributions and volume liquid water contents in broadband solar radiation computations follow the foregoing cases. In the thermal infrared radiation transfer analysis, all clouds are assumed to be black except cirrus depicted in cases 1, 12a, 13a and 14a.

In the cloud cover generation scheme described previously, there is a possibility that cloud cover values may differ from one layer to another in a multilayered cloud system. However, for the purpose of radiative transfer calculations in which clouds are considered to be plane-parallel, an averaged cloud cover value is utilized. The cloud geometric thickness in each case varies with respect to time and grid space. Thus, the vertical liquid water/ice content can be evaluated by $W = w\Delta z$, where w denotes the volume liquid water/ice content in g m^{-3} and Δz is the geometric thickness. The vertical liquid water/ice contents are required in the calculations of broadband solar reflection and transmission values as well as broadband infrared emissivity, reflectivity and transmissivity values for cirrus.

In the present cloud generation scheme, we have considered and incorporated some aspects of the cloud microphysics in terms of mean liquid water content and water droplet/ice crystal characteristics by means of examining the cloud location and development. The total cloud cover predicted by the model, as will be discussed in the results section, has been compared with the satellite infrared cloud picture. However, we do not have means to check the vertical cloud structure since such data bases simply do not exist at the present time. Even if the data sets had been available, it would be difficult to make a direct comparison because of the model layer structure. In spite of all these uncertainties, we must consider that the model performs physically and consistently subject to assumptions and approximations imposed. Within the limitations of the model performance, it appears feasible to gain physical insight into the importance and relevance of radiation processes on the cloud formation and large scale dynamic processes in terms of various time and space scales.

TABLE 1. Observed cloud microphysics data for five cloud types depicted in Fig. 2 including the particle radius range, mean radius r_m and liquid water content w.

Index*	Cloud type	r (μm)	r_m (μm)	w (g m^{-3})	Reference
1, 12a, 13a, 14a	Ci	200/60	—	0.0033	Heymsfield (1975)
2, 3, 6, 11a, 12b	As	1–15	5	0.28	Diem (1948)
4, 11b, 13b, 15b	St	1–20	6	0.78	Singleton and Smith (1960)
7, 14b	Cu	1–20	7	0.66	Durbin (1959)
9	Cb	1–70	20	2.50	Weickmann and aufm Kampe (1953)

* For cloud types 5, 8, 10 and 15a (same as 5), which are composed of ice crystals above and water droplets below, see text for explanations.

3. Radiation transfer scheme

a. Infrared radiation program

Formulations and parameterizations of thermal infrared radiation in clear atmospheres containing water vapor, carbon dioxide and ozone as well as relevant computational results have been given in our previous publications (Liou, 1980, Liou and Ou, 1981; Liou and Ou, 1983; and Ou and Liou, 1983). However, new schemes involving the infrared radiative interactions of cloud and air have been developed and designed for specific incorporation into the spectral general circulation model.

As described in Section 2c, while the present model allows clouds to form in four tropospheric layers, it suffices to consider a single or two-layered cloud system for the purpose of computing radiation fluxes and heating–cooling rates (see Fig. 2). As a general approach to evaluate infrared radiation fluxes, we shall consider a two-layered cloud system having a semitransparent and nonblack high cloud aloft coupled with a black cloud below. Let the infrared broadband emissivity, transmissivity and reflectivity for the high cloud be denoted as ϵ^c, t^c and r^c, respectively. For black clouds, we let $\epsilon^c = 1$ and $t^c = r^c = 0$ for simplicity of treating the infrared flux exchange. In a manner similar to, but not exactly the same as, the parameterization equations given by Liou and Ou (1981), we may express the upward and downward fluxes at a given level (Fig. 3) above the high cloud, between high and progressively lower clouds, and below the lower cloud.

For heights above the high cloud top, we have

$$F^{\downarrow}(z) = \int_{z_\infty}^{z} \sigma T^4(z')K(z' - z)dz', \tag{3.1}$$

$$\begin{aligned} F^{\uparrow}(z) = {} & r^c \int_{z_\infty}^{z_{t1}} \sigma T^4(z')K(z' + z - 2z_{t1})dz' \\ & + t^c\Big\{\sigma T_{t2}^4[1 - \epsilon^f(z_{b1} + z - z_{t1}, T_{t2})] \\ & + \int_{z_{t2}}^{z_{b1}} \sigma T^4(z')K(z - z_{t1} + z_{b1} - z')dz'\Big\} \\ & + \epsilon_{t1}^c \sigma T_{t1}^4[1 - \epsilon^f(z - z_{t1}, T_{t1})] \\ & + \int_{z_{t1}}^{z} \sigma T^4(z')K(z - z')dz', \qquad (3.2) \\ & z_{t1} < z < z_\infty, \end{aligned}$$

where K and ϵ^f denote, respectively, the kernel function and broadband emissivity defined by Liou and Ou (1983). Subscripts for T and z in Fig. 3 are selfexplanatory. Below the cloud base and above the low cloud top, we obtain

$$\begin{aligned} F^{\uparrow}(z) = {} & \sigma T_{t2}^4[1 - \epsilon^f(z, T_{t2})] \\ & + \int_{z_{t2}}^{z} \sigma T^4(z')K(z - z')dz', \qquad (3.3) \end{aligned}$$

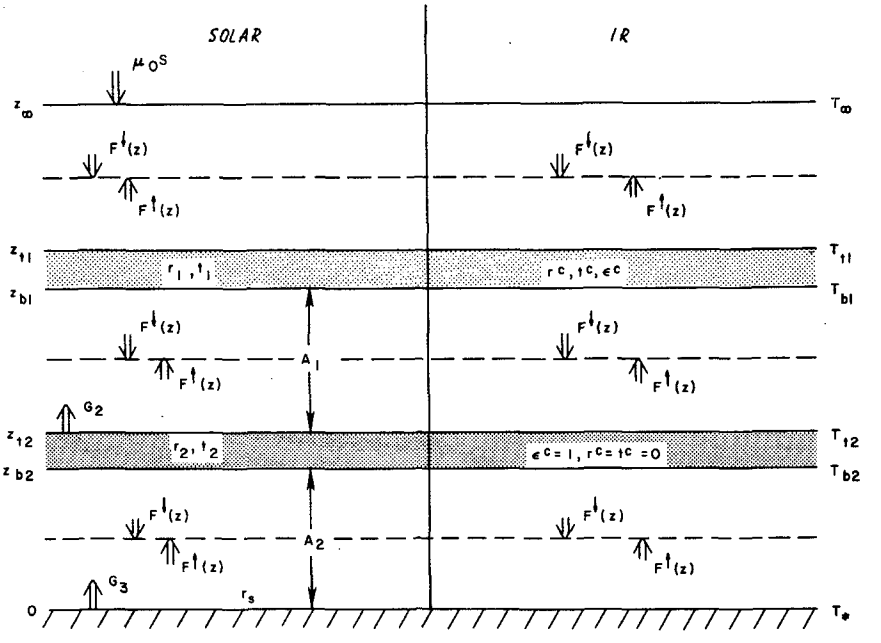

FIG. 3. Geometric configurations for the transfer of broadband solar and IR fluxes in an atmosphere containing two-layered clouds. All the notations are defined in the text.

$$F^{\downarrow}(z) = r^{c}\left\{\sigma T_{t2}^{4}[1 - \epsilon^{f}(2z_{b1} - z, T_{t2})] + \int_{z_{t2}}^{z} \sigma T^{4}(z')K(2z_{b1} - z - z')dz'\right\} + t^{c}\int_{z_{\infty}}^{z_{t1}} \sigma T^{4}(z')K(z' - z_{t1} - z_{b1} - z)dz' + \left\{\epsilon_{b1}^{c}\sigma T_{b1}^{4}[1 - \epsilon^{f}(z_{b1} - z, T_{b1})] + \int_{z_{b1}}^{z} \sigma T^{4}(z')K(z' - z)dz'\right\}, \quad (3.4)$$

$$z_{t2} < z < z_{b1}.$$

Below the low cloud base, the fluxes are related to two black surfaces and are simply given by

$$F^{\downarrow}(z) = \sigma T_{*}^{4}[1 - \epsilon^{f}(z, T_{*})] + \int_{0}^{z} \sigma T^{4}(z')K(z - z')dz', \quad (3.5)$$

$$F^{\downarrow}(z) = \sigma T_{b2}^{4}[1 - \epsilon^{f}(z_{b2} - z, T_{b2})] + \int_{z_{b2}}^{z} \sigma T^{4}(z')K(z - z')dz', \quad (3.6)$$

$$0 < z < z_{b2},$$

where T_{*} denotes the surface temperature.

The broadband infrared emissivity, reflectivity and transmissivity for cirrus are functions of the vertical ice content produced by the cloud generation scheme. Computations of these values in the dynamic model follow the parameterization equation developed by Liou and Wittman (1979). The cirrus broadband emissivity, which is a function of the vertical ice content, is directly proportional to the vertical geometric thickness generated in the model. It varies as a function of time and grid space but its values are normally less than 0.5.

When there is only one cloud generated in the model, we set $z_{b2} = z_{t2} = z_{b1}$ and $T_{b2} = T_{t2} = T_{b1}$. Thus, only Eqs. (3.1)–(3.4) are required in the computation. Note that except for single high clouds, all other cloud types are considered to be black radiatively. In the cases when clouds are formed in adjacent layers (Fig. 2, cases 5, 6, 7, 8, 9, 10, 14b and 15a), they are considered to be black single clouds in infrared flux calculations. In the black-cloud case, internal net infrared fluxes at the boundary of the model layer are obtained through a quadratic interpolation between the net fluxes at the top and bottom of the black cloud. It follows that infrared cooling rates can be evaluated in each model layer for all cloudy conditions. Moreover, when the model generates partial cloud cover over a grid cell, infrared cooling rates at each model layer for this grid cell are obtained by weighting linearly the fractional cloud cover, c, multiplying the cloudy infrared cooling rate and the percentage of the clear portion, multiplying the clear infrared cooling rate, i.e.,

$$Q_{\mathrm{IR}}^{pc} = cQ_{\mathrm{IR}}^{c} + (1 - c)Q_{\mathrm{IR}}^{nc}. \quad (3.7)$$

This equation is also applicable to the computation of solar heating rate Q_s in a partly cloudy condition.

The heating rate at level σ is related to the divergence of net fluxes and is given by

$$Q = \pm \frac{g}{P_{*}C_{p}} \frac{d[F^{\uparrow}(\sigma) - F^{\downarrow}(\sigma)]}{d\sigma}, \quad (3.8)$$

where P_{*} is the surface pressure, C_p the specific heat at constant pressure and the negative and positive signs stand for infrared and solar fluxes, respectively. Note that the net radiative heating/cooling $Q_R = Q_S + Q_{\mathrm{IR}}$.

b. Solar radiation program

Parameterizations of the transfer of broadband solar fluxes in Rayleigh atmospheres have been previously described in Liou and Ou (1983). In that paper, the broadband solar absorptivities for water vapor, carbon dioxide and ozone along with the Rayleigh scattering correction have been discussed in relation to upward and downward solar flux formulations.

As in the case of the infrared radiation program, we consider a general two-layered cloud system for the transfer of broadband solar fluxes. We wish to obtain the upward and downward solar fluxes at levels above the high cloud, between the high and low clouds and below the low cloud. Utilizing an approach similar to the flux transfer in a clear atmosphere and in reference to Fig. 3, the downward and upward solar fluxes above z_{t1} may be written in the form

$$F^{\downarrow}(z) = \mu_0 S_0[1 - A(z)], \quad (3.9)$$

$$F^{\uparrow}(z) = F^{\downarrow}(z_{t1})R_3[1 - \bar{A}(z - z_{t1})], \quad (3.10)$$

$$z > z_{t1},$$

where S_0 is the solar constant which is taken to be 1360 W m^{-2}, $\mu_0 = \sin\theta\cos\delta + \cos\theta\sin\delta\cos\Delta$ with δ and Δ denoting the solar inclination angle and hour angle, respectively, A represents the broadband solar absorptivity which is a function of the atmospheric path length expressed in the height coordinate, $\bar{A}$ is its diffuse value, R_3 is the solar flux reflection involving the two cloud system and the surface defined below, and $F^{\downarrow}(z_{t1})$ is the downward solar flux at position z_{t1}.

To derive the flux from below the high cloud, we let the solar flux reflection and transmission for the high (1) and low (2) clouds be (r_1, t_1) and (r_2, t_2), respectively, with their corresponding diffuse (or global) quantities denoted as $\bar{r}_1$, $\bar{t}_1$, $\bar{r}_2$ and $\bar{t}_2$ and let $\bar{A}_1$ and $\bar{A}_2$ be the diffuse gaseous absorption between the high and low clouds and between the low cloud and the surface. We also utilize a nondimensional diffuse gen-

eration function $G_2^{(t)}$ which is initiated from the reflection of the low cloud with a contribution from the surface to be defined below. Thus, the downward and upward fluxes between z_{b1} and z_{t2} may be written

$$F^{\downarrow}(z) = F^{\downarrow}(z_{t1})[t_1 + G_2^{(t)}(1 - \bar{A}_1)\bar{r}_1][1 - \bar{A}(z_{b1} - z)], \tag{3.11}$$

$$F^{\uparrow}(z) = F^{\downarrow}(z_{t1})G_2^{(t)}[1 - \bar{A}(z - z_{t2})], \tag{3.12}$$

$$z_{b1} > z > z_{t2}.$$

In Eq. (3.11), the t_1 term represents the direct transmission of the broadband solar flux reaching the high cloud top, while the following term denotes the diffuse component that is generated through the generation function $G_2^{(t)}$.

Similarly, if we let the direct transmission for the two cloud system be $\mathcal{T}_2$ (the corresponding reflection will be denoted by R_2) and the upward generation function originating from the surface by G_3, then the downward and upward fluxes below the low cloud base z_{b1} are described by

$$F^{\downarrow}(z) = F^{\downarrow}(z_t)\mathcal{T}_3[1 - \bar{A}(z_{b2} - z)], \tag{3.13}$$

$$F^{\uparrow}(z) = F^{\downarrow}(z_t)G_3[1 - \bar{A}(z)], \tag{3.14}$$

$$z_{b2} > z > 0,$$

where $\mathcal{T}_3$ denotes the direct transmission for the system of two clouds and the surface.

The derivation of the flux reflection and transmission and the upward generation function for multiple cloud layers is similar to but not exactly the same as the adding method for radiative transfer outlined in Hutchison and Liou (1982); Liou (1980, Chapter 6) and Hansen (1971). In this approach we postulate that the broadband solar flux either in the form of direct or diffuse beam is additive by means of multiple reflections between layers concerned. Thus, the flux reflection and transmission for two cloud layers are

$$R_2 = r_1 + G_2(1 - \bar{A}_1)\bar{t}_1, \tag{3.15}$$

$$\mathcal{T}_2 = t_1(1 - \bar{A}_1)t_2 + G_2(1 - \bar{A}_1)^2\bar{r}_1\bar{t}_2, \tag{3.16}$$

where the first and second terms represent, respectively, the direct and diffuse contribution with the latter resulted from the upward generation function from the low cloud layer given by

$$G_2 = t_1(1 - \bar{A}_1)r_2[1 - (1 - \bar{A}_1)^2\bar{r}_1\bar{r}_2]^{-1}; \tag{3.17}$$

here the last term denotes multiple reflections between two clouds. It follows that the reflection and transmission for a combination of two clouds and the surface is then given by

$$R_3 = R_2 + G_3(1 - \bar{A}_2)\bar{\mathcal{T}}_2^*, \tag{3.18}$$

$$\mathcal{T}_3 = \mathcal{T}_2 + G_3(1 - \bar{A}_2)\bar{R}_2^*, \tag{3.19}$$

where the upward generation function from the surface is

$$G_3 = \mathcal{T}_2(1 - \bar{A}_2)r_s[1 - (1 - \bar{A}_2)^2\bar{R}_2^* r_s]^{-1} \tag{3.20}$$

and $\bar{R}_2^*$ and $\bar{\mathcal{T}}_2^*$ are the diffuse reflection and transmission for the two cloud system when radiation is incident from below. Thus, Eqs. (3.15)–(3.17) may be modified to yield

$$\bar{R}_2^* = \bar{r}_2 + G_2^*(1 - \bar{A}_1)\bar{t}_2, \tag{3.21}$$

$$\bar{\mathcal{T}}_2^* = \bar{t}_2(1 - \bar{A}_1)\bar{t}_1 + G_2^*(1 - \bar{A}_1)^2 r_2\bar{t}_1, \tag{3.22}$$

$$G_2^* = \bar{t}_2(1 - \bar{A}_1)\bar{r}_1[1 - (1 - \bar{A}_1)^2\bar{r}_1\bar{r}_2]^{-1}. \tag{3.23}$$

Finally, in Eqs. (3.12) and (3.13), the total upward generation function contributed from the low cloud and the surface is

$$G_2^{(t)} = G_2 + G_3(1 - \bar{A}_2)\bar{t}_2[1 - (1 - \bar{A}_1)^2\bar{r}_1\bar{r}_2]^{-1}, \tag{3.24}$$

where the second term is required in order to have internal fluxes properly taken into consideration.

The broadband solar reflection and transmission values for various cloud types are obtained through the following parameterization equation based on detailed radiative transfer calculations:

$$r, t(\mu_0, W, \bar{T}) = \sum_{m=0}^{3}\sum_{n=0}^{3}[a_{mn}\mu_0^m W^n + (\bar{T} - \bar{T}_{\text{Ref}})b_{mn}\mu_0^m W^n], \tag{3.25}$$

where a_{mn} are empirical coefficients drived based on the parameterization principle proposed by Liou and Wittman (1979). Here, we have added a temperature correction term since the amount of saturation water vapor within the cloud depends on the cloud temperature which will affect cloud reflection and transmission properties to some degree. The empirical coefficients b_{mn} are derived based on a fitting procedure and $\bar{T}$ and $\bar{T}_{\text{Ref}}$ denote, respectively, the mean and reference temperatures of a cloud.

In the case when ice and water particles coexist in the cloud (cases 5, 8, 10, and 15a in Fig. 2), we use Eqs. (3.15) and (3.16) to get the reflection and transmission for the combined cloud system. This is quite important from the point of view of radiative transfer since ice clouds are normally semitransparent allowing large portions of solar flux to transmit through the cloud which will be subsequently reflected back by high reflecting lower water clouds. As a result, the combined ice and water cloud system will have a significantly large reflection value. Computations of solar heating rates in clear, overcast and partly cloudy conditions follow Eqs. (3.7) and (3.8). Finally, the surface albedo r_s for each grid cell is computed from the surface geographic map and albedo values for various land surfaces provided by Katayama (1966). For the water surface, the albedo is assumed to be 0.07.

4. Simulation results and physical discussions

a. Model computations

In Fig. 4, we present infrared cooling profiles for clear and all possible cloudy atmospheres produced by the model using a standard atmospheric temperature and water vapor profiles. For cloudy conditions, 100% cloud cover is assumed in the calculation. In a clear atmosphere, maximum cooling rates on the order of 2°C d^{-1} are seen near the ground. Another maximum is located at about 5 km due to the structure of temperature and water vapor profiles. Cooling rates decrease to a height of about 12 km and then increase as a function of height due to carbon dioxide and ozone absorption and emission. When a model cirrus is present, a maximum cooling rate of about 3°C d^{-1} is generated in the cloud layer. For two middle clouds, which are assumed to be black, maximum cooling rates are again generated in the cloud layers which suppress greatly the cooling below the clouds. Right below the cloud, slight warming is seen. Since the higher middle cloud is thicker than the lower middle cloud, due to the model layer structure, it has a smaller maximum than the latter. For the low stratus which is also assumed to be black, we see a large cooling generated by the relatively thin cloud. Because the cloud base temperature is very close to the surface temperature, insignificant heating–cooling is generated below the cloud. Note that the maximum cooling produced by black clouds is directly controlled by the cloud thickness through an inverse relationship.

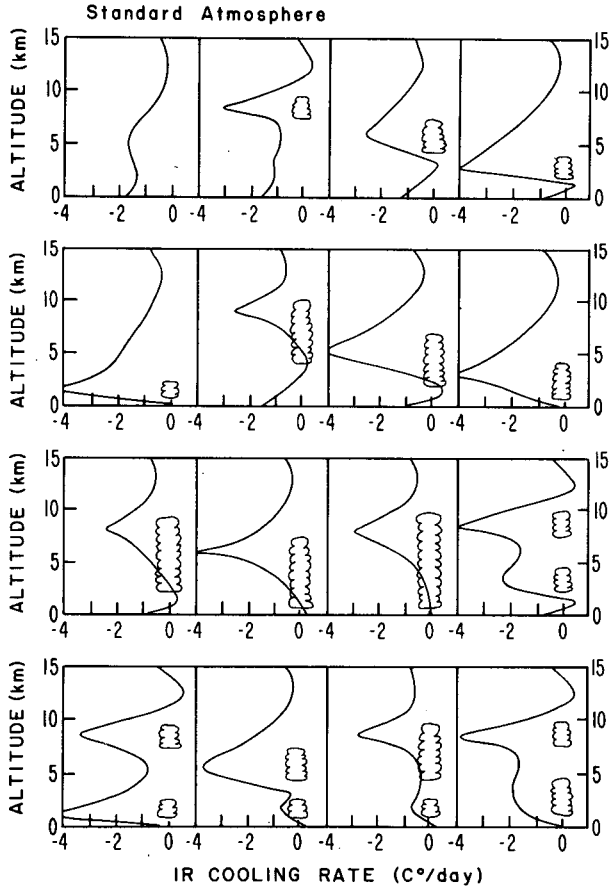

FIG. 4. Infrared cooling rate profiles for clear and all possible cloudy atmospheres produced by the model for standard atmospheric temperature and humidity profiles. 100% cloud cover is assumed in the calculation. Cooling rate profiles for partly cloudy conditions may be estimated by using Eq. (3.7).

For other single cloud systems which are composed of 2–4 cloud layers depicted in the figure, the general cooling rate profiles are similar to those for a single model cloud layer. However, the degree of cooling varies somewhat due to cloud thickness and cloud top temperatures which affect the cooling in the opposite direction. When two separate cloud systems are involved, two cooling rate maxima are generated as evidenced from the high–low or high–middle cloud combination. In the case of the middle–low cloud system cooling rates below the middle cloud are largely reduced since the middle cloud base and low cloud top temperatures differ only slightly.

The corresponding solar counterparts are depicted in Fig. 5. In these calculations, we employ a solar constant of 1360 W m^{-2}, a surface albedo of 0.15, a cosine of the solar zenith angle of 0.5 and a solar time duration of 12 h. Solar heating rates in a clear atmosphere are generally less than about 1°C per solar day below about 15 km. Solar heating rates within the cloud depend on the cloud absorptivity which in turn is a function of the cloud liquid water/ice content. For this reason, cirrus produces a small heating rate, while larger heating rates are produced by middle and low clouds. For a single cloud composed of high and other cloud layers, the maximum heating produced by the cloud become broadened. This is due to the fact that the high cloud in the system is treated separately with water clouds. A large portion of solar flux will transmit through it and be reflected back by the optically thick water cloud so that absorption within the high cloud is increased. Meanwhile, a certain portion of solar heating will also be available to the water cloud for absorption. As a result, these single cloud systems (5, 8, 10 and 15) have broad heating maxima. For water cloud cases, which may consist of two or three layers, there are only single heating maxima at the cloud top since most of the solar fluxes are either reflected back to the atmosphere above or absorbed within the higher cloud layer so that solar flux is not available for the progressively lower cloud layer. When high and middle–low clouds are separated by the atmosphere we see two distinct heating peaks because both clouds generate heating within.

The condition under which solar heating rates are calculated represents a mean climatological state and therefore may be directly compared with the infrared cooling profiles. In a clear atmosphere, cooling out-

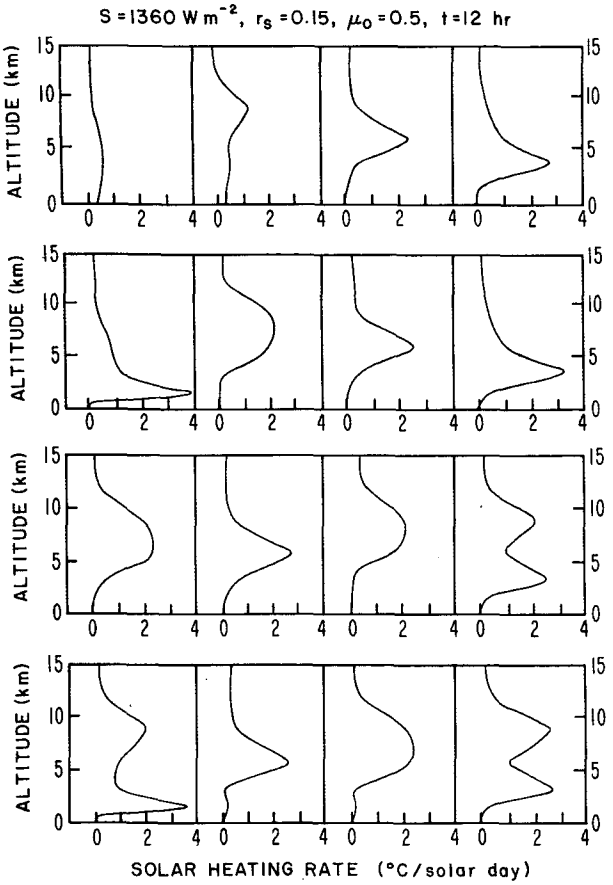

FIG. 5. Solar heating rate profiles for clear and all possible cloudy atmospheres produced by the model for standard atmospheric temperature and humidity profiles. These profiles should be compared directly with the IR counterparts depicted in Fig. 4.

weighs heating everywhere in the atmosphere with a net cooling rate on the order of 1°C d^{-1} in the troposphere. In various cloudy conditions, it is also the general tendency that maximum cooling rates are greater than the maximum heating rates. This is especially evident for high clouds where cooling is a factor of three larger than the warming. The quantitative effects of various vertical cloud combinations on the solar heating and IR cooling profiles with respect to those of a clear column (on the extreme left of the uppermost diagrams) under a standard atmospheric condition are evident from Figs. 4 and 5. The radiative heating and cooling within the cloud system is clearly associated with the cloud dynamic stability.

In Fig. 6 we show the calculated cloud cover over the western hemisphere on the initial day (6 June 1980) using the scheme described in Section 2c. The contour lines are plotted in an increment of 0.3 cloud cover beginning with an initial value of 0.2. For verification purposes, we also depict the GOES west IR cloud picture observed at the same time. The calculated cloud fields are in general agreement with the large cloud cover observed in the 0–15°N tropical region, the Atlantic Ocean and the north American continent. The calculated cloud cover is underestimated, however, in the tropical Pacific. By and large, the present cloud generation scheme appears to be physically adequate. The prime objective of this comparison is to examine whether the cloud cover generation scheme described in Section 2c is physically adequate. The computational results presented here do not involve the prediction of the large scale humidity and cloud field, however. We recognize that the analysis of the humidity field in any general circulation model presently available is generally unsatisfactory physically and dynamically. Nevertheless, it should be pointed out that the empirical coefficients contained in the critical relative humidity depicted in Eq. (2.29) are determined on the basis of adjusting the predicted cloud cover to the observed cloud cover from satellite sources (Geleyn, 1981). In addition, in the lowest diagram of the same figure, we also present the calculated IR fluxes at the top of the model layer corresponding to the calculated cloud fields and clear atmospheres. The IR flux contours are plotted in units of W m^{-2}. Low IR fluxes are generally associated with the cloud fields which normally have lower temperatures than the underlying surface as is apparent in the tropical region, Atlantic ocean and north American continent. Clear columns, on the other hand, emit larger IR fluxes due to the relatively warmer surface. This is especially evident in the area over the United States where we find the maximum emitting IR fluxes as large as 350 W m^{-2}. Unfortunately, we were unable to obtain the observed IR fluxes derived from the earth radiation budget experiment on this particular day. Comparisons of the calculated and available observed radiative fluxes at the top of the atmosphere will also provide a first order verification on the model performance. This is an area that we plan to explore in future experimentations.

b. Interactions between radiation, clouds and dynamic processes and the description of the numerical experiment

Indeed, radiation transfer processes involving solar and IR fluxes, the formation of clouds and large scale dynamic processes interact intricately with numerous possible feedbacks in the model atmosphere as is evident from Eqs. (2.3), (2.23), (2.24), (2.25), (2.27) and (2.28). Depicted in Fig. 7 is a systematic diagram illustrating the relationships of various dynamic and thermodynamic processes.

For the purpose of physically examining the effects of radiative processes in the atmosphere and at the land surface on the prediction of the vertical velocity, cloud cover and temperature fields, we have divided the present numerical experiment into two groups. The first includes the calculation of radiative flux exchanges, whereas the second excludes all radiative pro-

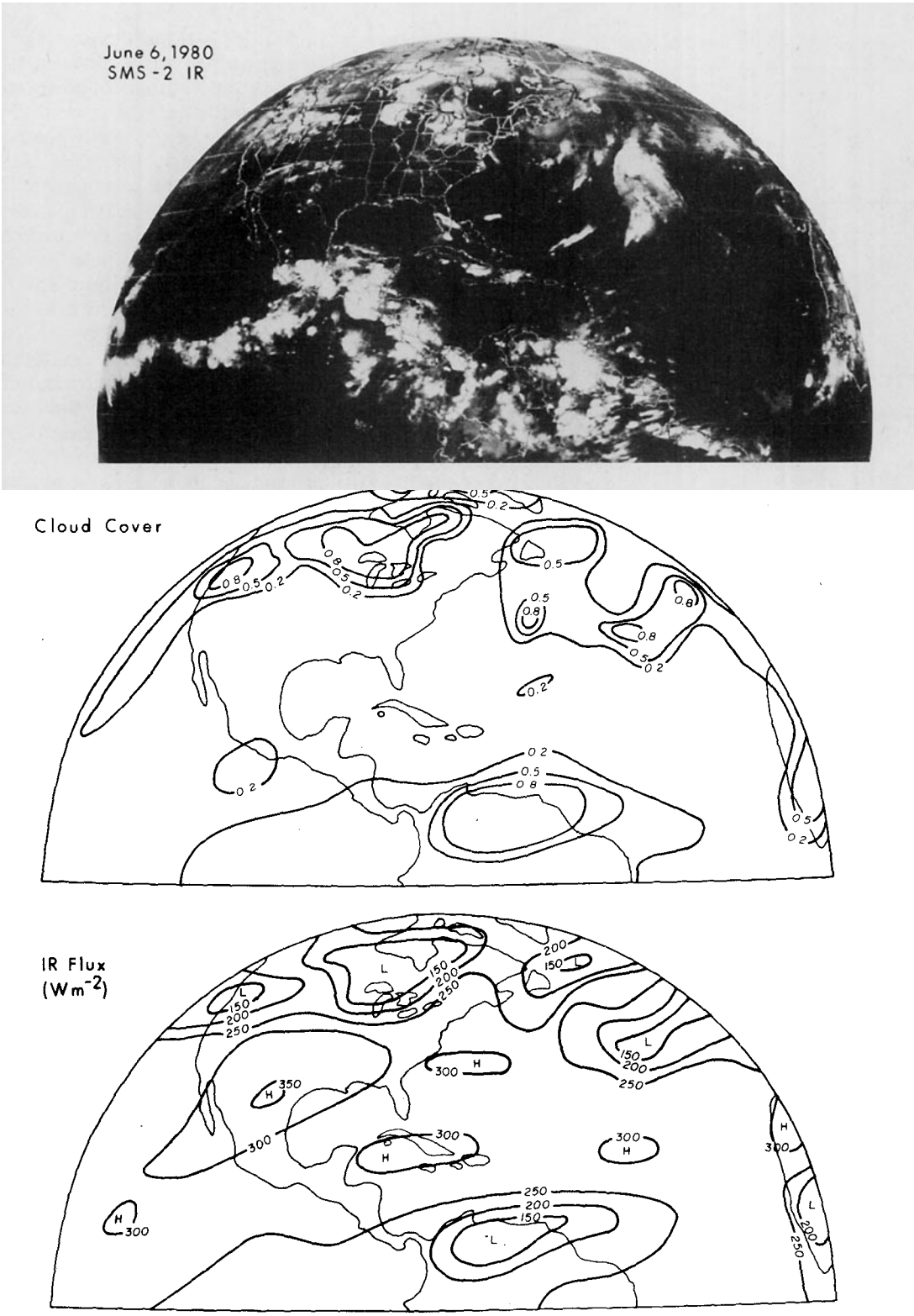

FIG. 6. The uppermost diagram represents the GOES west IR cloud picture. The middle diagram denotes the calculated cloud cover contour lines over the Western Hemisphere on the initial day, 6 June 1980. The lowermost diagram shows the contour lines for the corresponding outgoing IR flux at the top of the atmosphere in units of W m^{-2}.

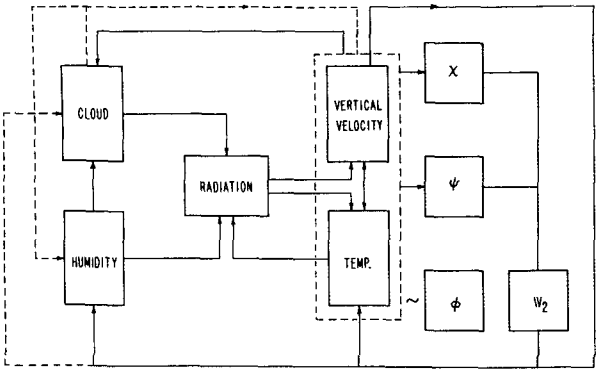

FIG. 7. A flow chart indicating the intricate relations between radiative processes, vertical velocity, temperature, humidity, clouds and large-scale horizontal motion. The solid and dashed lines represent, respectively, direct and indirect effects of various processes.

cesses in the experiment. In the former case, the land surface temperature is derived from Eq. (2.16) and the atmospheric heating and cooling rates produced by the transfer of solar and IR fluxes are calculated from the schemes reported in Section 3. In the later case when all radiative computations are removed from the model, we do not evaluate the land surface temperature from Eq. (2.16). Rather, we utilize the predicted atmospheric temperatures at $\sigma = 0.85, 0.97$. We then extrapolate/interpolate these temperatures to 1000 mb for presentation purposes. Moreover, as pointed out in Section 2a, the ocean temperatures are prescribed in the model. Without the incorporation of radiation programs for the atmosphere and land surface, the model will provide the prediction of the vertical velocity, cloud cover, temperature and other relevant variables.

With respect to the initialization of the input data for the present numerical integration, temperature, humidity and geopotential height fields and u and v components obtained from the conventional NMC objective analysis are used. Utilizing the nonlinear balance equation on the pressure coordinate, the stream function ψ may be evaluated (Zheng, 1981). Moreover, the conventional omega equation is used to estimate the vertical velocity. At this point, values of the temperature T, humidity q, the vertical velocity $\hat{\omega}$ and u_ψ and v_ψ are then interpolated to the σ-coordinate. From Eq. (2.8) and subsequently Eq. (2.20), $\dot{\sigma}$ and the velocity potential χ may be successively evaluated.

In the process of initialization for applications to numerical experimentations in the σ-coordinate, no diabatic forcing (radiation and latent heat) is included. Therefore, the two aforementioned experiments will begin with the same initial conditions. This is consistent with our objective of investigating the influence of radiative processes within the model on the predicted cloud cover and dynamic variables.

In order to gain physical insight into the quantitative contribution of radiative processes to the vertical velocity, we compute the vertical velocity with and without the inclusion of the radiative heating term as follows:

$$-\lambda a^2\nabla^2(a^2\dot{\sigma}_R^{t+\Delta t}) - \frac{\partial^2}{\partial\sigma^2}(a^2\dot{\sigma}_R^{t+\Delta t}) = \eta a^2\nabla^2 Q_R + \hat{F}_R, \tag{4.1}$$

$$-\lambda a^2\nabla^2(a^2\dot{\sigma}_E^{t+\Delta t}) - \frac{\partial^2}{\partial\sigma^2}(a^2\dot{\sigma}_E^{t+\Delta t}) = \hat{F}_E, \tag{4.2}$$

where $\eta = \Delta t^2 R/(\alpha\sigma)$, $\hat{F}_R$ represents all other terms except the term directly associated with the radiative heating Q_R through the term E^T denoted in Eq. (2.23) and $\hat{F}_E$ denotes the equivalent components without the contribution of Q_R. In the numerical computation we note that $\dot{\sigma}_R = \dot{\sigma}_E = 0$ when $\sigma = 0$ and 1. In addition, we define $\Delta\dot{\sigma} = \dot{\sigma}_R - \dot{\sigma}_E$ which represents a physical quantity indicating the nonlinear contribution of radiative heating to the vertical velocity.

To understand the direct effect of the radiative heating–cooling on the temperature prediction, we carry out the following computations:

$$T_R^{t+\Delta t} = T_R^t + 2\left(\frac{\partial T}{\partial t}\right)_R^t \Delta t, \tag{4.3}$$

$$T_E^{t+\Delta t} = T_E^t + 2\left(\frac{\partial T}{\partial t}\right)_E^t \Delta t, \tag{4.4}$$

where the heating and cooling rates at time step t from Eq. (2.3) may be written

$$\left(\frac{\partial T}{\partial t}\right)_R = -\frac{u}{a\sin\theta}\frac{\partial T}{\partial\lambda} - \frac{v}{a}\frac{\partial T}{\partial\theta} + \left(\frac{RT}{C_p} - \frac{\partial T}{\partial\sigma}\right)\dot{\sigma}_R + \frac{RT}{C_p}\frac{d\ln P_*}{dt} - \frac{FL}{C_p a^2}\delta_R\hat{\omega}_R + Q_R + F^T + \frac{g}{P_*}\frac{\partial\tau^T}{\partial\sigma}, \tag{4.5}$$

$$\left(\frac{\partial T}{\partial t}\right)_E = -\frac{u}{a\sin\theta}\frac{\partial T}{\partial\lambda} - \frac{v}{a}\frac{\partial T}{\partial\theta} + \left(\frac{RT}{C_p} - \frac{\partial T}{\partial\sigma}\right)\dot{\sigma}_E + \frac{RT}{C_p}\frac{d\ln P_*}{dt} - \frac{FL}{C_p a^2}\delta_E\hat{\omega}_E + F^T + \frac{g}{P_*}\frac{\partial\tau^T}{\partial\sigma}. \tag{4.6}$$

Clouds in the model are generated from the humidity field through the empirical equation denoted in Eq. (2.27) in which the temperature information is needed. In a manner similar to the foregoing analysis, the effect of radiative processes on the prediction of the humidity distribution may be understood from the following equations:

$$\left(\frac{\partial q}{\partial t}\right)_R = -\frac{u}{a\sin\theta}\frac{\partial q}{\partial\lambda} - \frac{v}{a}\frac{\partial q}{\partial\theta} - \dot{\sigma}_R\frac{\partial q}{\partial\sigma} + \frac{F}{a^2}\delta_R\hat{\omega}_R + F^q + \frac{g}{P_*}\frac{\partial\tau^q}{\partial\sigma}, \tag{4.7}$$

$$\left(\frac{\partial q}{\partial t}\right)_E = -\frac{u}{a\sin\theta}\frac{\partial q}{\partial \lambda} - \frac{v}{a}\frac{\partial q}{\partial \theta} - \dot{\sigma}_E\frac{\partial q}{\partial \sigma} + \frac{F}{a^2}\delta_E\hat{\omega}_E + F^q + \frac{g}{P_*}\frac{\partial \tau^q}{\partial \sigma}. \quad (4.8)$$

It is clear that radiative processes affect the variation of the humidity field indirectly via the vertical velocity.

The latent heat release during the cloud formation with and without the contribution from radiative processes may be denoted by

$$L_R = -\frac{FL}{C_p a^2}\delta_R\hat{\omega}_R, \quad (4.9)$$

$$L_E = -\frac{FL}{C_p a^2}\delta_E\hat{\omega}_E. \quad (4.10)$$

Following the numerical experiment described previously, we have carried out prediction of the vertical velocity, cloud cover, temperature and geopotential height field for nine consecutive days. Prediction results are then compared with available NMC data covering the period 7 to 15 June 1980 (6 June is the initial day). Since the fundamental objective of the present study is to examine quantitatively and understand physically the interactions of various physical and dynamical processes, we have decided not to present detailed results in terms of statistical analyses and model skill. Moreover, we have selected a complete set of prediction results for the fifth day to illustrate the intricate interactions of atmospheric radiative flux exchanges with cloud formation and dynamic processes. The rationale and the physical basis for such a selection is as follows. By virtue of conventional knowledge, it is physically understood that the effects of radiative processes on the short-range weather prediction within three days in terms of large-scale parameters are not pronounced and significant in view of the longer relaxation of radiative transfer in a dynamic and thermodynamic system. On the other hand, however, it is generally recognized dynamically that the prediction accuracy of the large-scale flow pattern and temperature fields deteriorates and the state of prediction collapses beyond about five to six days, using the currently available numerical models. In addition to the consideration of these two aspects, our choice of the fifth day results for presentation is also based on our physical and dynamical understanding of the present model behavior as well as comprehensive analyses of the prediction results. However, we are not suggesting here that this selection is the best one for other numerical simulations.

A brief discussion of the model performance with radiation programs included is in order. In addition to the fifth day results to be presented below, we have carried out the analysis of the correlation coefficient γ between the predicted and observed temperature changes at middle levels. Using the observed NMC data covering a ten-day period (6–15 June 1980), it is shown that γ approaches about 66% at day nine at which time the forecast errors are less than the persistence errors. Futhermore, we have also analyzed the globally averaged geopotential height rms errors at 300 mb with and without the consideration of radiative processes in the prediction. We found that when radiation is included in the model calculation, the predicted rms errors after day 5 are less than those without the inclusion of radiation computations by about 1 to 4 m with an averaged value of about 3 m.

In the next subsections we shall describe the predicted vertical velocity, cloud cover and temperature and assess the associated radiation contributions.

c. *Effects of radiative processes on the vertical velocity*

It is commonly understood in the modeling of the large-scale motion that the vertical velocity prediction is essential to the success of the temperature and geopotential height prediction. The distinct feature of the present model which differs from other GCMs is the manner in which the solution of the vertical velocity is derived and computed. We illustrate in Eq. (4.1) that the computation of the vertical velocity can be decomposed into the Laplacian of the radiative heating–cooling rate and other dynamic and thermodynamic sources. In this subsection we wish to investigate the quantitative effects of radiative processes on the predicted large-scale vertical velocity distribution. Note that the time step employed in the model is 30 min and the wavenumber expansion along the latitude is 17. For one day prediction, the computer time required is about 2 min in the Cray-1 computer.

Figure 8 depicts the predicted zonally averaged net radiative heating for the Northern Hemisphere on day five (11 June 1980). It is quite evident that infrared cooling rates outweigh solar heating rates everywhere in the atmosphere. In the tropical region, the atmosphere near the surface shows a maximum cooling rate due to the large concentration of water vapor. In the region between 700 and 500 mb, another cooling maximum is also observed. This maximum is basically

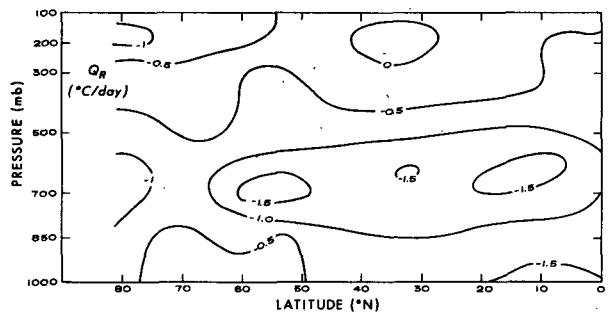

FIG. 8. The predicted net radiative heating–cooling rate profile zonally averaged for the Northern Hemisphere on day five, 11 June 1980.

caused by the cloud top infrared cooling in agreement with large low and middle cloud covers predicted from the model. Low and middle clouds also suppress cooling beneath so that a distinct pattern involving two cooling maxima is shown. In the upper troposphere and lower stratosphere, cooling is generally small due to small water vapor and ozone concentrations. A broad cooling peak located at 200 mb is a result of the strong cooling from the high cloud top. In the latitude between about 20 and 50°N, which is an area of subsidence, atmospheric cooling is uniformly small due to less frequent cloud activities. Between 50–70°N, a cooling maximum is seen at about 700 mb which corresponds again to the large cloud cover generated by the baroclinic instability of the atmosphere. Near the surface, there is also a weak cooling maximum. The broad peak at about 300 mb is again due to the high cloud top cooling in space. The inhomogeneous distribution of atmospheric cooling due to radiative processes in the vertical as well as horizontal directions affects the computation of the vertical velocity in a manner discussed below.

In Fig. 9 are shown the predicted vertical velocity zonal profiles at day five with (lower diagram) and without (upper diagram) the inclusion of the radiative heating–cooling rate calculations. The units for the vertical velocity are in 10^{-4} mb s^{-1} and the upward (−) and downward (+) motions are indicated in the diagram. In reference to the upper diagram, the maximum upward motion is observed at 10°N near about 600 mb, while the downward motion is seen at 30°N. This constitutes the Hadley circulation in the tropical region. The sinking air rises gradually and shows a small maximum at ~ (750 mb, 40°N). When it reaches ~60°N, the upward motion intensifies with a maximum greater than 1.2×10^{-4} mb s^{-1}. On both sides of this maximum, downward motions are observed with maxima located at about 50 and 70°N. These patterns constitute the basic meridional circulation in middle latitudes and another Hadley cell in high latitudes. When the radiative heating–cooling processes are incorporated in the model calculations, the fundamental vertical velocity patterns do not alter significantly but there are a number of noticeable modifications. As illustrated in the lower diagram, the upward motion maximum denoted at ~ (400 mb, 10°N) shifts toward the equator and the adjacent upward motion fields intensifies by almost a factor of 2. This intensification is in accord with the net radiative cooling pattern in the tropics depicted in the previous figure. In particular, we note that the distinct vertical gradient of cooling is found at ~10°N. Moreover the upward and downward motions located at about 60 and 50°N, respectively, appear to increase slightly in magnitude, indicating the possibility of the intensification of the meridional circulation. On inspection of Eq. (4.1) and in reference to Eq. (4.2) we find that the vertical velocity computation is related to the Laplacian of the radiative heating rate. Thus, we interpret the increase of the vertical velocity gradient by horizontal and vertical differentials of radiative cooling at latitudes from 50 to 70°N and relatively uniform cooling profiles at latitudes from 40 to 50°N. It is quite evident, however, that radiative flux exchanges in the tropics lead to a significant intensification of the Hadley circulation and that such processes also strengthen somewhat the meridional circulation, both of which appear to be closely associated with the cooling produced in the cloud top areas described previously.

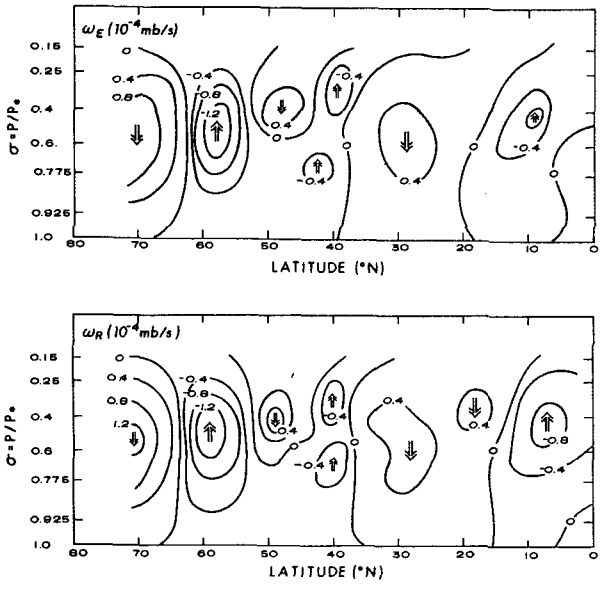

FIG. 9. The predicted vertical velocity zonally-averaged profiles with (lower diagram) and without (upper diagram) the inclusion of the radiative heating–cooling calculations in the model on day 5, 11 June 1980. The units for the vertical velocity are in 10^{-4} mb s^{-1}. Upward and downward motions are indicated in these diagrams.

In conjunction with the vertical velocity profile, it appears interesting to examine the possible radiative effect on the latent heat release. We depict in Fig. 10 the latent heat profile according to definitions given in Eqs. (4.9) and (4.10). Latent heat release is directly related to the cloud formation and therefore is restricted in the four σ layers ranging approximately from 850 to 300 mb. In reference to the upper chart where radiative heating–cooling were not included in the model calculations, there are three distinct centers for latent heat distributions which correspond approximately to the formation of large cloud covers in the tropics, the baroclinic zone and the arctic region. Radiative exchanges, primarily infrared fluxes, intensify the latent heat releases significantly in the tropics where the maximum increases by about a factor of two (from 0.4 to 0.7°C d^{-1}). The intensifications are also noted in the latitudinal zones from 40 to 60°. It seems quite clear that these increases in the latent heat release are associated with enlargements of the upward vertical velocity fields at about 10 and 60°N depicted in Fig. 9. It is also interesting to compare the relative magnitude

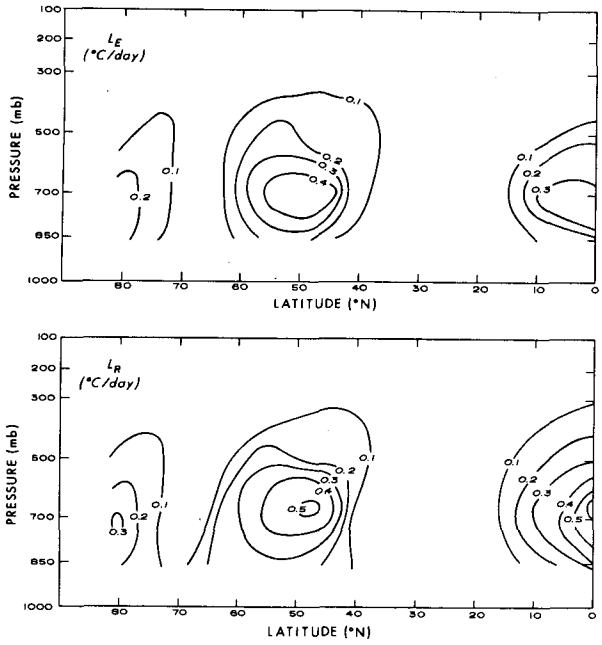

FIG. 10. The predicted latent heat zonally-averaged profiles with (lower diagram) and without (upper diagram) the incorporation of the radiative heating–cooling calculations in the model on day five, 11 June 1980.

of L_R and Q_R (Fig. 8). As shown, radiative cooling rates caused by the domination of infrared flux exchanges are larger than the heating produced by changes of the thermodynamic phase of water vapor molecules. Vertical eddy transports bring some of the excess solar fluxes absorbed by the surface to the atmosphere, balancing the net cooling in the atmosphere to some degree. The present model probably underestimates the latent heat release in the upper tropical atmosphere. This is in view of the fact that the formation of tropical clouds follow the empirical scheme described in Subsection 2C without a special consideration of cumulus dynamics. Also note that the present model is a hemispheric model and because of the restriction of the boundary condition, the latent heat release close to the equator would be underestimated.

In Fig. 11 we present the model predicted vertical velocity ω_R at 600 mb for day five and the difference of the vertical velocity $\Delta\omega = \omega_R - \omega_E$ where ω_E represents the vertical velocity when radiative processes were not included in the numerical experiment. $\Delta\omega$ therefore represents the part of the vertical velocity generated from radiative processes. The heavy solid lines denote the regions where the vertical velocity is zero. The positive and negative signs represent, respectively, the downward and upward motions and the isopleths are plotted in every 3×10^{-4} and 2×10^{-4} mb s^{-1} for ω_R and $\Delta\omega$, respectively.

In the middle and high latitudes, ω_R shows a distribution of positives and negatives along the latitude. These patterns are closely associated with the temperature and wind fields. On day three (9 June, not shown here) the model predicts a strong temperature trough in the east part of north America. The vertical velocity gradient in this region is correspondingly strong. After the third day the strength of the vertical velocity is weakened and the patterns break into numerous small centers on the fifth day corresponding to the decrease of the temperature gradient. In addition, we also observe the eastward movement of the strong vertical velocity center along the east part of Asia. Normally, when a strong temperature trough presides, ω_R patterns show relatively strong positive and negative centers. In the Gulf of Mexico, the model predicts very realistic cloud cover patterns in day five (see Fig. 13). We find that the upward vertical velocity distribution in this region generally coincides with the cloud distribution.

The lower chart in Fig. 11 shows the distribution of $\Delta\omega = \omega_R - \omega_E$ on 600 mb. As pointed out previously, $\Delta\omega$ is the part of the vertical velocity produced by radiative processes through various nonlinear interactions. In addition to the direct influence illustrated in the first term on the right-hand side of Eq. (4.1), radiative processes denoted by Q_R indirectly affect the vertical velocity calculation via temperature, clouds and humidity loops as demonstrated in Fig. 7. These direct and indirect impacts are related to the spatial distribution of the temperature, humidity and clouds. Consequently, $\Delta\omega$ shows a distribution of positives and negatives along the latitude, especially along middle and high latitudinal circles. In the tropics, $\Delta\omega$ is especially closely associated with the cloud distribution. The maximum for $\Delta\omega$ in middle and high latitudes is on the order of 2×10^{-4} mb s^{-1} which is about 10–15% of the corresponding ω_R value. However, in the tropical region, we find that $\Delta\omega$ and ω_R values have about the same magnitudes. Specifically, in the Gulf of Mexico, $\Delta\omega$ distributions are almost identical to ω_R distributions illustrated in the upper chart. It appears, therefore, that radiative processes have profound and direct impacts on the vertical velocity in the tropical region which in turn affects large-scale dynamic processes.

In the course of attempting to understand the influence of radiative processes on large-scale synoptic features by means of their contributions to the vertical velocity computation, a consistent and characteristic pattern was discovered. Depicted in the middle and lower charts of Fig. 12 are the predicted 700 and 500 mb temperature and geopotential height fields for the region covering about 80–40°N and 120–180°E on 11 June 1980. The upper chart illustrates the corresponding vertical velocity ($\Delta\omega$) that is produced by radiative processes at the 600 mb surface. Around the Kamchatka peninsula and its northern areas, we observe from both 700 and 500 mb charts that there was a strong warm advection of temperature. Clouds were predicted in these areas from the model. An inspection

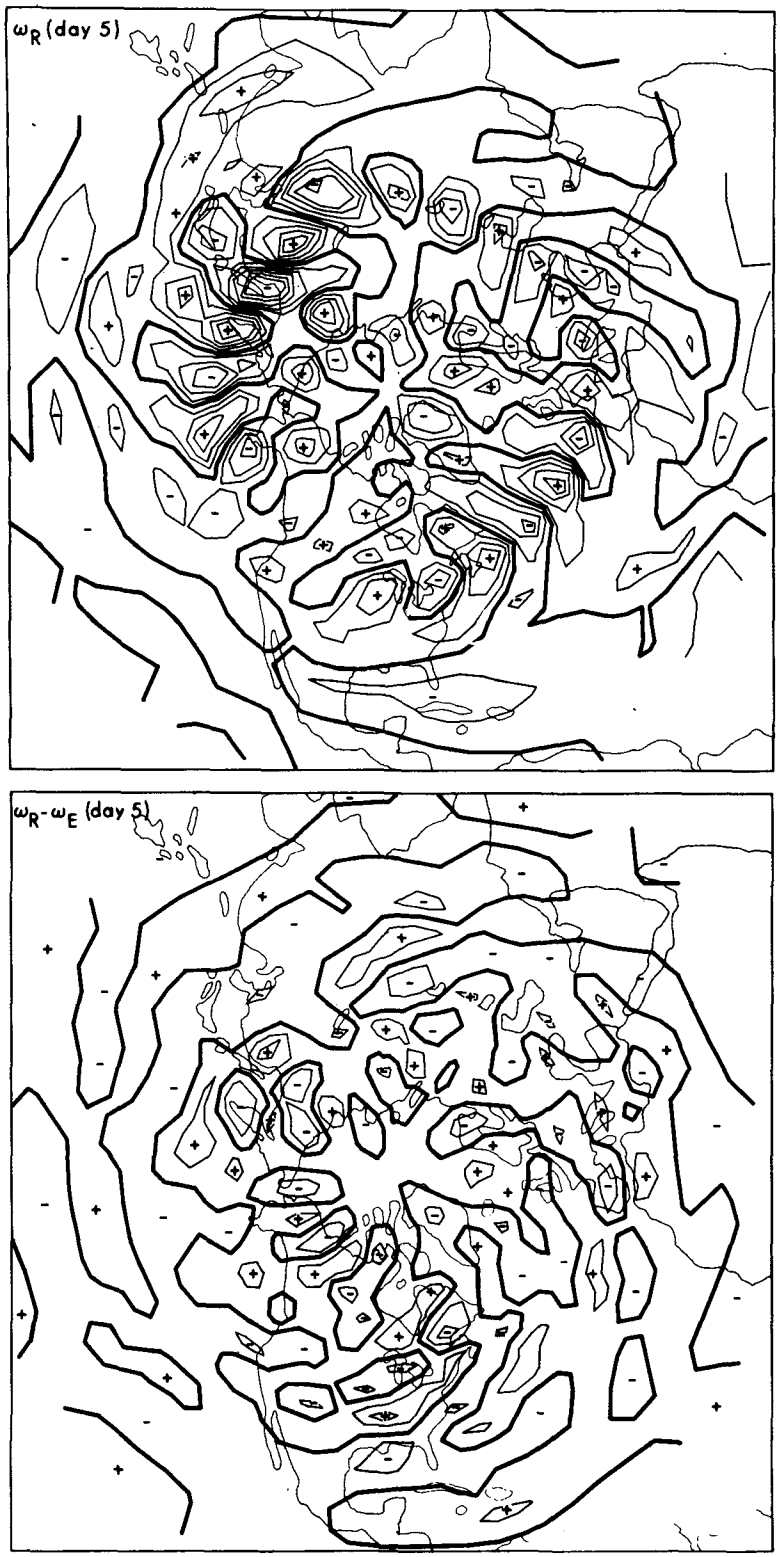

FIG. 11. The predicted 600 mb vertical velocity ω_R (upper chart) and the difference of the vertical velocity ($\omega_R - \omega_E$), where ω_E represents the predicted vertical velocity when radiative processes are not included in the model experiment (lower diagram). The heavy lines denote the regions where the vertical velocity is zero. The positive and negative signs represent, respectively, the downward and upward motions and the isopleths are plotted in every 3×10^{-4} and 2×10^{-4} mb s^{-1} for ω_R and ($\omega_R - \omega_E$) respectively.

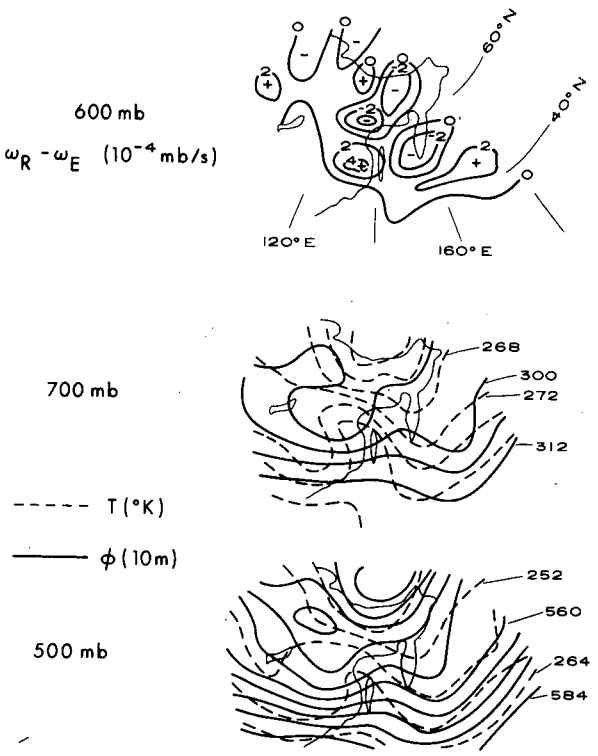

FIG. 12. The upper chart illustrates the part of the vertical velocity produced by radiative processes at 600 mb. The middle and lower charts show the predicted 700 and 500 mb temperature and geopotential height fields for the region covering about 40–80°N and 120–180°E on 11 June 1980.

of the vertical velocity chart reveals that radiative processes enhance the upward motion by virtue of the cloud top-cooling and base-warming mechanism. The area from the Baykal lake to Kuril islands, however, is dominated by a cold advection of temperature which is also seen on both 700 and 500 mb charts. Cloud-free atmospheres were generally predicted from the model. Here, radiative flux exchanges tend to suppress the upward motion and/or enhance the downward motion and therefore would tend to stabilize the atmosphere where the cooling rate has its largest values near the surface. The patterns of advection of high and low temperature in relation to the radiatively enhanced vertical velocity appear characteristic on the basis of a number of cases analyzed. This leads us to review the flow chart illustrated in Fig. 7 where we see that the large-scale motion affects the humidity distribution from which clouds are produced. Clouds, on the other hand, are the most dominant components in the radiation field of the atmosphere and drastically modify heating and cooling features, especially at cloud tops and bases. The subsequent effects on the vertical velocity have been demonstrated in the preceding discussion.

In this subsection, we have demonstrated and documented the relative importance of radiative processes on the vertical velocity computation and have attempted to understand physically and quantitatively some of the intricate interactions and plausible feedbacks between radiation and dynamic processes in light of the model results.

d. Effects of radiative processes on the cloud and temperature prediction

In this subsection, we wish to examine in an orderly manner the quantitative effects of radiative processes on the prediction of cloud distributions and temperatures.

In Figs. 13b and c, the cloud cover predicted from the model on day five is shown (white areas). Fig. 13b is with radiation included in the model calculation, whereas Fig. 13c depicts results without the inclusion of radiation programs in the prediction calculation. For verification purposes, the IR cloud picture derived from the NOAA polar orbiting satellite is depicted in Fig. 13a. Note that the predicted cloud cover values match the time of the IR cloud picture. Figs. 13b and c are obtained by shading the cloud cover values greater than 20%. As shown in Fig. 13b, the predicted cloud cover generally reproduces fairly closely the cloud systems in the tropics associated with the intertropical covergence zone. In the middle latitudes, the frontal cloud over the east coast of the United States is predicted correctly. The cloud systems over Asia and the eastern Pacific are also reproduced quite well from the model. Over the Arctic, large cloud cover is seen from the satellite and the predicted cloud cover appears to compare reasonably well. When radiation programs were removed from the model, the predicted cloud cover does not change significantly over the arctic regions. However, the predicted cloud cover is underestimated by as much as 50% in the tropical Pacific and Atlantic Oceans.

There appears to be two compelling reasons as to why the cloud cover is largely underestimated in the tropics when radiation calculations were not carried out in the model prediction. First, as shown in Eq. (2.27), when the predicted relative humidity is less than or equal to a critical value no cloud is allowed to form. Moreover, the relative humidity is computed from the ratio of the predicted mixing ratio to the saturation mixing ratio which is a function of the temperature only. As pointed out in Subsections 4a and 4b, infrared cooling generally outweighs solar heating everywhere in the atmosphere. This is especially evident for the tropical night when solar radiation is not available. Thus, the saturation mixing ratio will be generally a relatively larger value in the case of no radiation, whereas it will be a smaller value in view of the domination of atmospheric infrared cooling effects. As a result, the model restricts the formation of clouds in the case of no radiation since the predicted relative humidity will be relatively small. Second, radiative flux transfer contributes quite importantly to the ver-

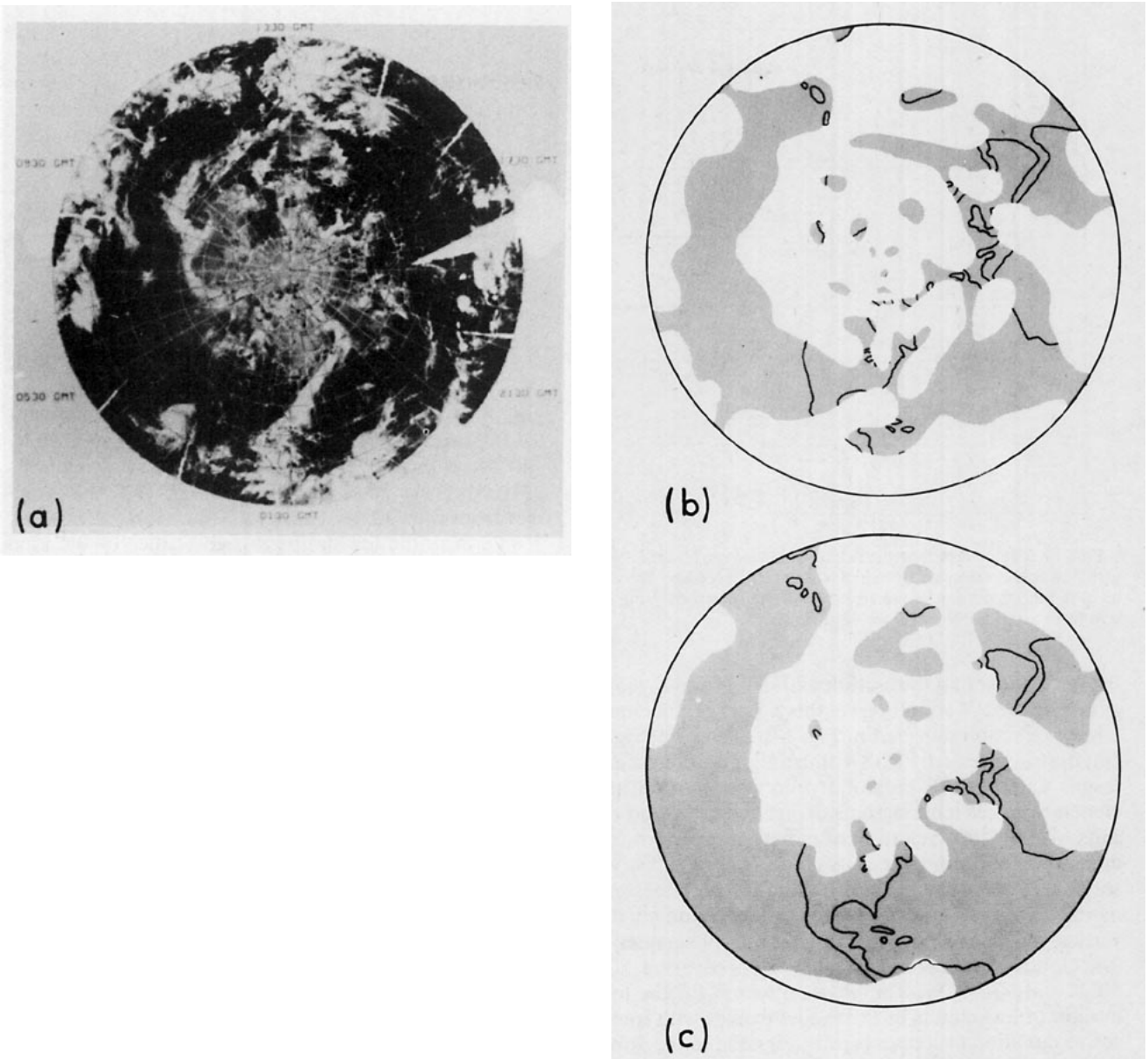

FIG. 13. (a) The IR cloud picture from the NOAA satellite on 11 June 1980. (b) The cloud cover (white areas) predicted from the model on day five, 11 June 1980 with radiative programs included in the model. (c) As in (b) except without the inclusion of radiation programs in the prediction computation.

tical velocity component as demonstrated in Fig. 11. This contribution will also lead to a positive increase in the cloud cover prediction through the cloud cover correction and to less magnitude in the mixing ratio prediction described in Eq. (4.7). In this equation, local time rate of change of water vapor mixing ratio is basically controlled by the large scale atmospheric motion. The indirect contribution of the radiation component via the vertical velocity is generally secondary. In sum, and in reference to Fig. 7, radiative flux exchanges in the model atmosphere will have a positive feedback for the cloud formation through the vertical velocity and temperature box.

In addition to the cloud cover prediction, we present in Fig. 14 the predicted vertical cloud structure with and without the inclusion of radiation processes in the model. Unfortunately, we do not have the observed cloud type and layered structure for comparison with the predicted values. Nevertheless, it seems vitally significant to examine physically the influence of radiative heating and cooling in the atmosphere on the formation of the vertical cloud structure. We do so by selecting

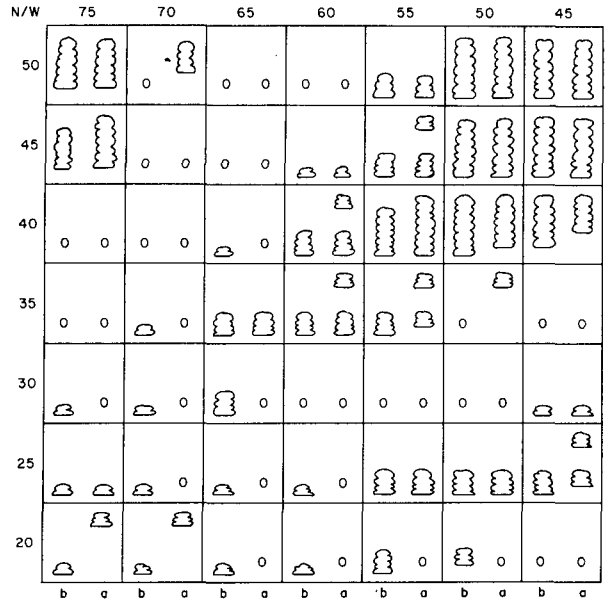

FIG. 14. The predicted vertical cloud structure on 11 June 1980 with (left column denoted by b) and without (right column denoted by a) the incorporation of radiative transfer programs covering an area from 20 to 50°N and from 45 to 75°W.

the region covering the latitudes 20–50°N and the longitude 45–75°W which represents a part of the cloud cover prediction depicted in Fig. 13b and c. The right cloud structures in Fig. 14 illustrate the prediction results under which radiation processes were not included, whereas left diagrams depict vertical cloud results with the incorporation of radiation programs. As demonstrated in the previous cloud cover figures, we see that in the tropical region, radiative processes enhance the cloud cover prediction. Inspection of the vertical structure shows that these clouds are generally low clouds as evidenced in the region covering 20–30°N and 60–75°W. The physical reason for the formation of low clouds in the model tropics with interactive radiation processes is primarily due to the domination of infrared cooling in the lower atmosphere described previously. However, the production of high clouds in the model which permits radiative energy exchanges is less frequent. This is evident in middle latitudes where we see the disappearance of high clouds when radiative processes were taken into consideration in the model. In the region between 45–50°W and 45–50°N, the atmosphere apparently was extremely unstable due to large-scale dynamic factors so that with and without the inclusion of radiation the formation of clouds in the four model layers was not affected significantly.

The prime objective of a numerical weather prediction model is to perform short and medium range forecasts and to achieve and provide reliable predictions in terms of large-scale temperature and geopotential height fields. In line with this objective, we first demonstrate in Fig. 15 the zonally averaged temperature errors defined as the differences between predicted and observed temperatures for 11 June 1980. The observed temperature data sets are available through conventional NMC objective analyses. The upper chart depicts these errors when radiation programs were not incorporated in the model experiment. The largest error, on the order of ~3°C, is found from 30 to 40°N near the surface, and from 60 to 70°N close to 300 mb. The former is an underestimation while the latter is an overestimation. We also observe that the predicted temperatures are underestimated by about 2°C at ~ (35°, 200 mb) and ~ (70°, 1000 mb). In reference to the results depicted in the lower chart when radiative heating–cooling calculations were included in the model, we find that there are noticeable improvements in the predicted temperature field. Specifically, the aforementioned maximum error centers located at 30–40°N and 60–70°N latitudes are reduced by about 1–2°C. Improvements (<1°C) are also noted in the tropics from 0 to 30°N.

To examine the statistical significance of the temperature prediction presented in Fig. 15, we have carried out the following analysis. We define three rms values in the form

$$\mathrm{rms}_0 = \left\{\frac{1}{N}\sum_{j=1}^{N}[T_{0_j}^{(1)} - T_{0_j}^{(5)}]^2\right\}^{1/2}, \quad (4.11a)$$

$$\mathrm{rms}_E = \left\{\frac{1}{N}\sum_{j=1}^{N}[T_{E_j}^{(5)} - T_{0_j}^{(5)}]^2\right\}^{1/2}, \quad (4.11b)$$

$$\mathrm{rms}_R = \left\{\frac{1}{N}\sum_{j=1}^{N}[T_{R_j}^{(5)} - T_{0_j}^{(5)}]^2\right\}^{1/2}, \quad (4.11c)$$

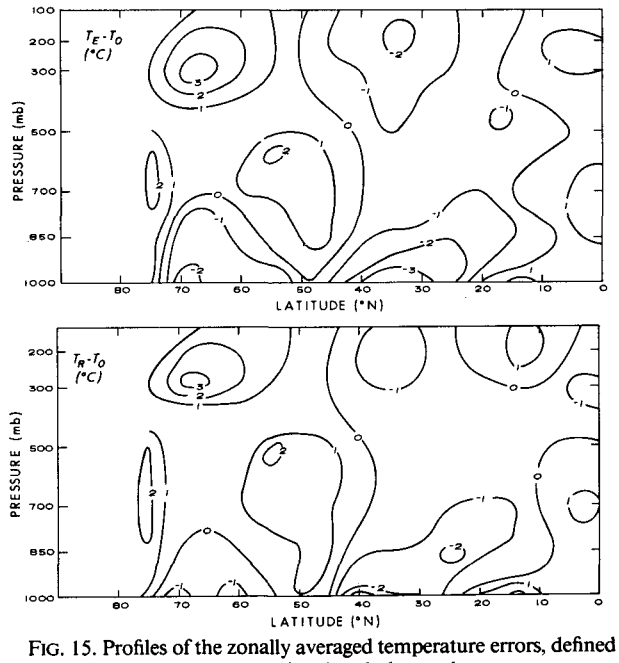

FIG. 15. Profiles of the zonally averaged temperature errors, defined as the differences between predicted and observed temperatures, on 11 June 1980. The lower and upper diagrams depict these errors with and without the inclusion of radiation programs.

where the sub-index j denotes the latitude and the super-indexes (1) and (5) denote, respectively, the initial (6 June 1980) and the fifth day (11 June 1980). T_0, T_E and T_R as defined previously represent, respectively, the temperatures derived from observations, predicted from the model without radiation and predicted from the model with radiation.

In Table 2 we list these values for a number of pressure levels. In general, temperatures predicted from the model are uniformly better than those from persistence. With the radiation–cloud program included in the model, we see a significant improvement of the temperature field in lower levels. This is especially evident for 1000 mb where an rms improvement of 0.36 K is shown. In high levels, however, the rms improvement of the predicted temperature due to the inclusion of radiation–cloud programs is generally small.

We have also carried out the computation of the daily variance of zonal mean temperature in terms of the absolute difference of the observed temperatures for the fifth (11 June) and fourth (10 June) days, i.e., $|T_{0_j}^{(5)} - T_{0_j}^{(4)}|$. The hemispheric average of this difference is 0.61 K with latitudinal averages of 1.04, 0.56, 0.38 and 0.51 for 1000, 850, 700 and 500 mb levels, respectively. In addition, we have calculated the absolute difference of the values presented in Figs. 15a and 15b. The hemispheric average of this difference is 0.35 K with latitudinal averages of 0.60, 0.28, 0.18 and 0.26 for 1000, 850, 700 and 500 mb levels, respectively. It is evident from these values that the differences in temperatures between these two figures are smaller than the daily variance defined previously.

Finally, we demonstrate in Fig. 16 the 500 mb temperature fields in the northern hemisphere predicted from the model (mean a) with verifications from observed data (mean b) covering a period from 7 to 15 June 1980. These charts represent the mean temperatures for nine consecutive days. In mean b, it is seen that northern Greenland is dominated by a strong trough which is gradually weakened southward along the Great Lakes and northeastern United States. Over the northern part of the Canadian coast, there is a strong ridge coupled with a broad trough in the south. A weak ridge and a rather intense trough are seen to be located over the central and eastern Atlantic ocean, respectively. There are also activities of weak wave motions in eastern Asia and Pacific ocean. The systematic distribution of the temperature troughs and ridges are accurately predicted by the present model, although the predicted low temperature center over Greenland is somewhat weaker.

TABLE 2. The rms temperatures (K) defined in Eqs. (4.11) for a number of pressure levels.

	Pressure (mb)			
	1000	850	700	500
rms_0	2.28	1.77	1.46	1.60
rms_E	1.68	1.12	1.01	0.85
rms_R	1.32	0.99	0.97	0.83

5. Conclusions

In this paper we have investigated the intricate relationship between radiation, clouds and dynamic processes employing a seven-level spectral general circulation model designed for short and medium range

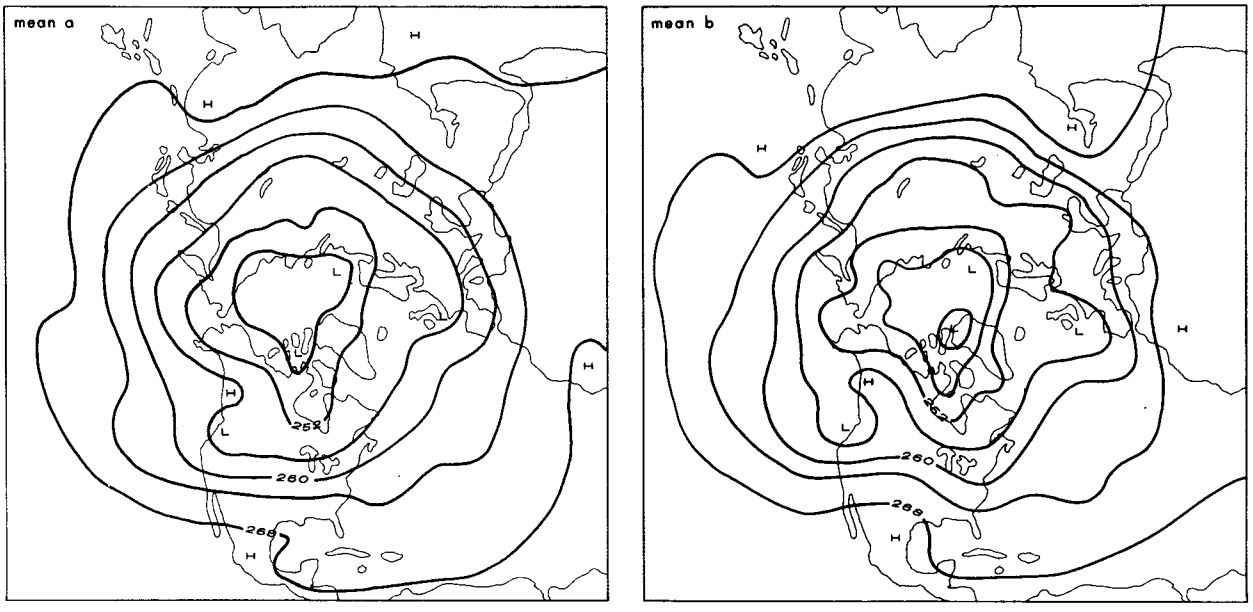

FIG. 16. Mean temperature charts (9-day mean, 500 mb) in the Northern Hemisphere predicted from the model (left) with verifications from the observed data (right) covering a period from 7 to 15 June 1980.

prediction. The distinct dynamic feature of the present model which differs from other GCMs is the manner in which the solution of the vertical velocity is derived and computed. We show that the computation of the vertical velocity may be decomposed into the Laplacian of the radiative heating rate and large-scale dynamic and thermodynamic factors.

Integration of a newly developed radiation and cloud parameterization program into the present general circulation model has been carried out from which quantitative contributions of radiative processes to the vertical velocity, temperature and cloud distributions are determined. Clouds are generated from an empirical and physical scheme via predicted relative humidity distributions. Cloud types are assigned in accordance with the physical locality of the formation. Calculations of the cloud liquid water content involving various cloud combinations for radiative transfer analyses are based on assumed particle size distributions for cumulus, stratus, altostratus, cumulonimbus and cirrus.

The radiative transfer parameterization scheme utilizes the concept of the broadband flux transfer in clear and cloudy atmospheres. The broadband IR emissivity and solar absorptivity for a mixture of water vapor, ozone and carbon dioxide are obtained from results published in a number of previous papers. In line with the gaseous broadband absorptivity, we have derived broadband solar flux reflection and transmission for various cloud types as functions of the liquid water content, solar zenith angle and average cloud temperature under a number of model conditions. Furthermore, high clouds are considered to be nonblack with their emissivities parameterized in terms of the vertical ice content.

By virtue of the fundamental equations governing the vertical velocity, temperature and cloud field (through the water vapor mixing ratio) in the general circulation model, the direct and indirect effects of radiative processes on these predicted variables are described. Highlights of the present numerical experiment on the interactions between radiation, clouds and dynamic processes are summarized below:

1) That radiative flux exchanges in the tropics lead to a significant intensification of the Hadley circulation and that such processes also strengthen in some degree the meridional circulation. These conclusions are based on the analysis of the predicted vertical velocity for the fifth day.

2) That the part of the vertical velocity produced by radiative processes is a significant component in the tropics whereas it is only about 10–15% of the total in middle and high latitudes within the context of the present model.

3) That radiative flux exchange processes appear to enhance and suppress the upward motion in areas associated with warm and cold temperature advections, respectively.

4) That the present model appears to perform reliably on the prediction of cloud cover with verification from the satellite IR cloud picture for the period from 7 June to 12 June 1980 and that the cloud cover in the tropics would have been underestimated by as much as 50% if radiative processes were not accounted for in the model.

5) That the present model with interactive radiative-cloud processes has improved the prediction of zonally averged temperatures on the fifth day by about 1–2°C in middle latitudes and 1°C in the tropics and that it predicts accurately the mean of the 500 mb temperatures for nine consecutive days utilizing an observed data set covering the period from 7 to 15 June 1980 for comparison. The improvement is shown to be significant statistically at 1000 and 850 mb.

In light of the present numerical experiment it appears that an appropriate and consistent integration of IR and solar radiative processes in general circulation models may lead to significant improvements on the performance of the model and the prediction of large-scale temperature distributions.

The present model has taken into consideration some aspects of the cloud microphysics by means of examining the cloud geometric location and development. It follows that condensation processes from which the percentage of cloud cover for each model layer is evaluated is related to the vertical liquid water content. This relationship is based on two empirical procedures involving the cloud cover prediction and the use of observed cloud microphysics data. The objective of the liquid water content calculations is primarily for the analysis of thermal infrared and solar flux transfer. However, model clouds and the associated liquid water contents do not evolve with respect to the time scale. It appears very difficult to incorporate physical and dynamic mechanisms for the formation and dissipation of individual clouds since activities of most clouds and/or cloud systems are subgrid-scale phenomena. Clearly, all types of clouds need to be physically parameterized in terms of large scale dynamic and hydrological variables consistent with the model structure. This is certainly an area requiring significant research effort in the future, especially when climate problems are involved.

In this paper, we have not specifically presented the distribution of precipitation which is also computed in the model assuming that all of the condensed water vapor is to fall instantly. Under this crude approximation, the precipitation per unit area in a time period may be estimated by the proper time and height integrations of the total time rate of change of the saturation mixing ratio which is directly related to the product of the vertical velocity $\hat{\omega}$ and the thermodynamic factor F introduced in Section 2a via a delta function defining the critical mixing ratio. Thus, condensation and precipitation processes are mathematically correlated by the critical relative humidity. Since the precipitation prediction is not the focus of the present investigation, we have neglected this aspect entirely in the paper. This is also in view of the fact

that reliable observed precipitation data for the period of our study were not available. The link between the liquid water content and precipitation in the present model is difficult to trace mathematically and physically, although both quantities are determined from condensation processes. To the extent that only limited and fortunate cloud populations could produce measurable precipitation at the surface, a direct parameterization of precipitation from the available liquid water content data would appear to be a better physical approach than from condensation. In any event, the relationship between condensation, liquid water content and precipitation, which are closely associated with radiative processes within the atmosphere and at the surface, needs to be parameterized physically and mathematically in a consistent manner. Certainly, this is an important subject which should be resolved in future numerical models.

In line with the present study, it would be interesting to examine the effects of radiative processes on the large-scale motion, through the vertical velocity computation as proposed in this paper, for a longer period of time, say on the order of one month. In addition, it would also be important to investigate the direct and indirect impacts of radiation–cloud processes induced by orography, such as the Tibetian Plateau, on the general circulation of the atmosphere with respect to various time scales utilizing a realistic general circulation model.

Acknowledgments. This research was supported in part by the Division of the Atmospheric Sciences, National Science Foundation, under Grant ATM-81-09050 and by the Air Force Geophysics Laboratory under Contracts F19628-81-K-0042 and F19628-83-K-0015. All the computations were carried out through the Cray-1 Computer in the National Center for Atmospheric Research, which is sponsored by the National Science Foundation. S. C. Ou, S. Kinne and K. Hutchison have contributed to the insertion of radiation programs into the present spectral general circulation model during the earlier stages of the research work. We also thank Drs. A. Kasahara and W. Washington of NCAR for their encouragement and moral support on our numerical experiments. Sharon Bennett is thanked for typing and editing several versions of the manuscript.

REFERENCES

Bourke, W., B. McAvaney, K. Puri and R. Thurling, 1977: Global modeling of atmospheric flow by spectral methods. *Methods in Computational Physics,* Vol. 17, *General Circulation Models of the Atmosphere,* J. Chang, Ed., Academic Press, 267–324.

Diem, M., 1948: Messungen der Frosse von Wolkenelementen II. *Meteor. Rundsch.,* **9,** 261–273.

Durbin, W. G., 1959: Droplet sampling in cumulus clouds. *Tellus,* **11,** 202–212.

Geleyn, J. F., 1981: Some diagnostics of the cloud/radiation interaction in ECMWF forecast model. *Workshop on Radiation and Cloud–Radiation Interaction in Numerical Modeling,* 135–162. [Available from European Centre for Medium Range Weather Forecasts.]

Hansen, J. E., 1971: Multiple scattering of polarized light in planetary atmospheres. Part I: The doubling method. *J. Atmos. Sci.,* **28,** 120–125.

Heymsfield, A., 1975: Cirrus uncinus generating cells and the evolution of cirroform clouds. Part I: Aircraft observations on the growth of the ice phase. *J. Atmos. Sci.,* **32,** 799–808.

House, R. A., Jr., and C. P. Chang, 1981: Inclusion of mesoscale updrafts and downdrafts in computations of vertical fluxes by ensembles of tropical clouds. *J. Atmos. Sci.,* **38,** 1751–1770.

Hutchison, K., and K. N. Liou, 1982: Parameterization of broadband solar radiation transfer in clear and cloudy atmospheres. Sci. Rept., AFGL-TR-82-0364, 110 pp. [Available from Air Force Geophysics Laboratory.]

Katayama, A., 1966: On the radiation budget of the troposphere over the northern hemisphere: I. Introduction. *J. Meteor. Soc. Japan,* **44,** 381–401.

Kuo, H. L., and Y. F. Qian, 1981: Influence of the Tibetian Plateau on cumulative and diurnal changes of weather and climate in summer. *Mon. Wea. Rev.,* **109,** 2337–2356.

Liou, K. N., 1980: *An Introduction to Atmospheric Radiation.* Academic Press, 392 pp.

——, and T. Sasamori, 1975: On the transfer of solar radiation in aerosol atmospheres. *J. Atmos. Sci.,* **32,** 2166–2177.

——, and G. D. Wittman, 1979: Parameterization of the radiative properties of clouds. *J. Atmos. Sci.,* **36,** 1261–1273.

——, and S. C. Ou, 1981: Parameterization of infrared radiative transfer in cloudy atmospheres. *J. Atmos. Sci.,* **38,** 2707–2716.

——, and ——, 1983: Theory of equilibrium temperature in radiative-turbulent atmospheres. *J. Atmos. Sci.,* **40,** 214–229.

Manabe, S., J. Smogorinsky and J. L. Holloway, Jr., 1979: Climate simulations with GFDL spectral models of the atmosphere: Effect of spectral truncation. Report of the JOC Study Conference on Climate Models: Performance, Intercomparison and Sensitivity Studies, Washington, DC, *GARP Publ. Ser.,* No. 22, 41–94 [NTIS N8027917].

Orszag, S. A., 1970: Transform method for the calculation of vector-coupled sums: Application to the spectral form of the vorticity equation. *J. Atmos. Sci.,* **27,** 890–895.

Ou, S. C., and K. N. Liou, 1983: Parameterization of carbon dioxide 15 μm absorption and emission. *J. Geophys. Res.,* **88,** 5203–5207.

Pitcher, E. J., R. C. Malone, V. Ramanathan, M. L. Blackmon, K. Puri and W. Bourke, 1983: January and July simulations with a spectral general circulation model. *J. Atmos. Sci.,* **40,** 580–604.

Ramanathan, V. E., E. J. Pitcher, R. C. Malone and M. L. Blackmon, 1983: The response of spectral general circulation model to refinements in radiative processes. *J. Atmos. Sci.,* **40,** 605–630.

Singleton, F., and D. F. Smith, 1960: Some observations of drop size distributions in low layer clouds. *Quart. J. Roy. Meteor. Soc.,* **86,** 454–467.

Smagorinsky, J., 1963: General circulation experiments with the primitive equations. I. The basic experiment. *Mon. Wea. Rev.,* **91,** 99–165.

Weickmann, H. K., and H. J. aufm Kampe, 1953: Physical properties of cumulus clouds. *J. Meteor.,* **10,** 204–211.

Wetherald, R. T., and S. Manabe, 1980: Cloud cover and climate sensitivity. *J. Atmos. Sci.,* **37,** 1485–1510.

Zheng, Q., 1979: A three-level filtered spectral model for northern hemisphere. *Acta Meteor. Sin.,* **37,** 36–43 (in Chinese).

——, 1980: A seven-level primitive equation spectral model. Collection of papers, *The Second (1977) National Numerical Weather Prediction Symposium,* 13–24, Science Press (in Chinese).

——, 1981: A four-level primitive equation spectral model and its application to the numerical weather prediction. *Sci. Sin.,* **24,** 1121–1132.